

12-1-2022

Hydrogeologic Heterogeneity Identification: Using Inverse Modeling of Synthetic Borehole Temperatures to Predict Groundwater Flux

Kevin Heintz

Follow this and additional works at: <https://digitalscholarship.unlv.edu/thesesdissertations>



Part of the [Geology Commons](#)

Repository Citation

Heintz, Kevin, "Hydrogeologic Heterogeneity Identification: Using Inverse Modeling of Synthetic Borehole Temperatures to Predict Groundwater Flux" (2022). *UNLV Theses, Dissertations, Professional Papers, and Capstones*. 4590.

<http://dx.doi.org/10.34917/35777472>

This Thesis is protected by copyright and/or related rights. It has been brought to you by Digital Scholarship@UNLV with permission from the rights-holder(s). You are free to use this Thesis in any way that is permitted by the copyright and related rights legislation that applies to your use. For other uses you need to obtain permission from the rights-holder(s) directly, unless additional rights are indicated by a Creative Commons license in the record and/or on the work itself.

This Thesis has been accepted for inclusion in UNLV Theses, Dissertations, Professional Papers, and Capstones by an authorized administrator of Digital Scholarship@UNLV. For more information, please contact digitalscholarship@unlv.edu.

HYDROGEOLOGIC HETEROGENEITY IDENTIFICATION: USING INVERSE
MODELING OF SYNTHETIC BOREHOLE TEMPERATURES TO
PREDICT GROUNDWATER FLUX

By

Kevin M. Heintz

Bachelor of Science – Geology
Northern Arizona University
2015

A thesis submitted in partial fulfillment
of the requirements for the

Master of Science – Geoscience

Department of Geoscience
College of Sciences
The Graduate College

University of Nevada, Las Vegas
December 2022



Thesis Approval

The Graduate College
The University of Nevada, Las Vegas

September 16, 2022

This thesis prepared by

Kevin M. Heintz

entitled

Hydrogeologic Heterogeneity Identification: Using Inverse Modeling of Synthetic Borehole Temperatures to Predict Groundwater Flux

is approved in partial fulfillment of the requirements for the degree of

Master of Science – Geoscience
Department of Geoscience

Mark Hausner, Ph.D.
Examination Committee Chair

Alyssa Crittenden, Ph.D.
*Vice Provost for Graduate Education &
Dean of the Graduate College*

David Kreamer, Ph.D.
Examination Committee Member

Michael Nicholl, Ph.D.
Examination Committee Member

Alexander Barzilov, Ph.D.
Graduate College Faculty Representative

ABSTRACT

Heat has been effectively used as a groundwater tracer for decades, and high-resolution temperature data can better identify and quantify discrete flow zones. Refinements to the numerical modeling of advective heat transfer in borehole temperature sensing deployments can improve understanding of dynamic hydrogeologic systems. In my thesis, I develop a novel two-dimensional coupled radial groundwater flow and heat transfer numerical model that considers intra-borehole vertical flow. To test the performance of this model, I used finite element analysis to generate synthetic data sets consisting of prescribed variable flow fields and resulting borehole temperatures. I input synthetic temperatures into the two-dimensional model and invert temperatures to optimize for horizontal flux. I compared prescribed synthetic flux and temperature with inverse model computed flux and temperature to determine the errors, limitations, and reliability of this approach. The inverse model predictably approximated the prescribed flow rate within a range of optimized flux (between $1.4\text{e-}6$ m/s [0.12 m/day] and $1.0\text{e-}5$ m/s [0.89 m/day]), and the inverse flux was greater than the prescribed flow rate by about a factor of two. I find that model predictions were affected by a systematic error attributed to modeling mechanics that biased inverse flux and, in part, limited the range of reliable flux calculations. The error between inverse and synthetic temperature was low and relatively consistent for all scenarios, except for conduction-dominated (i.e., low flow) cases. My study provides insights into several complexities associated with quantifying groundwater flow using heat transport as well as highlights the importance of vertical flow observations and synthetic data to refine and validate numerical models.

ACKNOWLEDGEMENTS

I would like to acknowledge my advisor, Dr. Mark Hausner, for providing continued support and guidance throughout this project. I also appreciate the feedback and mentoring I received from my committee members. I would like to acknowledge the Division of Hydrologic Sciences at Desert Research Institute for support and partial funding. Finally, I would like to thank my family for their perpetual encouragement, understanding, and love, especially my mother, Christi Heintz, whose passion for natural science continues to inspire.

TABLE OF CONTENTS

ABSTRACT.....	iii
ACKNOWLEDGEMENTS.....	iv
LIST OF TABLES.....	vi
LIST OF FIGURES.....	vii
1. INTRODUCTION.....	1
2. PREVIOUS WORK.....	2
3. METHODS.....	9
4. RESULTS.....	27
5. DISCUSSION.....	36
6. CONCLUSION.....	44
APPENDIX A: Details of model assumptions used for synthetic advection models.....	45
APPENDIX B: Temperature comparison curves of models that include vertical flow.	47
REFERENCES CITED.....	54
CURRICULUM VITAE.....	58

LIST OF TABLES

Table 1: Darcy fluid flow assumptions used in the synthetic FEA model.....	18
Table 2: Heat transfer assumptions used in the synthetic FEA model.	19
Table 3: Constants and assumptions used in the inverse model.	21
Table 4: Constants and assumptions used in the horizontal advection thermal diffusivity evaluation models.	22
Table 5: Synthetic FEA model scenarios.....	24
Table 6: Synthetic FEA prescribed hydraulic conductivity, intrinsic permeability, formation flux, and formation seepage velocity.	25
Table 7: Mean flow rate error and scenario averaged <i>RMSE</i> for model iterations to determine the best-fit thermal diffusivity.	28
Table 8: Computed inverse flux as compared to prescribed synthetic flow rates.	34
Table 9: Scenario averaged temperature difference and <i>RMSE</i> between synthetic and inverse temperatures.....	40
Table 10: Darcy fluid flow assumptions and justifications used in the synthetic FEA model.	45
Table 11: Heat transfer assumptions and justification used in the synthetic FEA model.....	46

LIST OF FIGURES

Figure 1: Numerical modeling approaches to radial heat transfer in a one-dimensional borehole cross-section.....	6
Figure 2: Energy terms used in numerical modeling.....	13
Figure 3: Dynamic variables in the numerical modeling of discretized borehole cylinders.	14
Figure 4: Plots of synthetic model flow scenarios.....	25
Figure 5: Temperature time series of model calculated heat transfer in a conduction-only regime.	28
Figure 6: Synthetic model generated plots of the horizontal flow scenario (v1).....	30
Figure 7: Temperature time series comparison of synthetic and inverse temperatures in the horizontal flow scenario (v1).....	32
Figure 8: Computed inverse flux and prescribed synthetic flux and seepage velocity at various hydraulic conductivities.....	35
Figure 9: Mean flow rate error associated with computed inverse flux and prescribed synthetic seepage velocity at various hydraulic conductivities.....	35
Figure 10: Mean temperature difference between prescribed synthetic temperature and computed inverse temperature for all eight model scenarios.	39
Figure 11: Temperature time series of model calculated heat transfer in model scenario v2.	47
Figure 12: Temperature time series of model calculated heat transfer in model scenario v3.	48
Figure 13: Temperature time series of model calculated heat transfer in model scenario v4.	49
Figure 14: Temperature time series of model calculated heat transfer in model scenario v5.	50
Figure 15: Temperature time series of model calculated heat transfer in model scenario v6.	51
Figure 16: Temperature time series of model calculated heat transfer in model scenario v7.	52
Figure 17: Temperature time series of model calculated heat transfer in model scenario v8.	53

1. INTRODUCTION

Identification of discrete zones of high groundwater flow can improve understanding of local groundwater systems and enable flow quantification at small (sub-meter) scales. Knowledge of these zones can refine estimations of contaminant migration, better predict depths for water supplies, and assess well construction issues. Numerical groundwater models are used to characterize hydrogeologic systems by simulating groundwater flow through hydrostratigraphic units with unique geometry and flow properties using governing hydraulic equations. These models require input of known or assumed parameters such as hydrologic and hydraulic properties and external constraints (e.g., initial and boundary conditions). Field measurements—including groundwater temperature—that quantify aquifer properties are critical for model development and improve the accuracy with which flow is estimated.

This thesis presents a method for interpreting continuous temperature data collected with distributed thermal perturbation sensing, in which numerical modeling of aquifer temperature is used to predict groundwater flow. I review previous studies that introduce the theoretical basis for my modeling approach, discuss my coupled groundwater flow and heat transfer numerical model, and present the synthetic simulations of variable groundwater flow and temperature that I used to characterize model performance. I evaluate the capabilities and limitations of the model through comparisons between modeled and synthetic results. This approach provides a refinement to the numerical modeling of advective heat transfer in groundwater temperature sensing deployments that can improve discrete flow identification and advance understanding in complex hydrogeologic systems.

2. PREVIOUS WORK

This section provides a brief history of using heat as a tracer in groundwater systems, and the evolution from temperature observations applied in seminal studies to a quasi-one-dimensional radial model of heat transfer used to evaluate a continuous temperature sensing experiment in an aquifer.

Heat as a Tracer for Groundwater Flow

Temperature changes in groundwater are controlled by the fundamental properties of heat transport, which provide mechanisms to relate heat to groundwater flow. Groundwater heat has been used as a flow tracer for decades beginning with temperature modeling to predict vertical flow near the surface (Suzuki, 1960; Stallman, 1965) and in deeper applications (Bredehoeft and Papadopulos, 1965), which was applied at aquifer scales (Cartwright, 1970; Taniguchi et al., 2003) and led to quantifiable flow in two dimensions (Lu and Ge, 1996). Transient temperature observations at high spatial resolution facilitated dynamic sensing (Selker et al., 2006; Tyler et al., 2009), where discrete zones of flow became identifiable (Read et al., 2013; Banks et al., 2014; Hausner et al., 2016).

Conduction and advection control heat transfer in saturated porous media, where conduction depends on the porosity (i.e., moisture content) and thermal conductivity of the rock matrix and the fluid (Anderson, 2005; Domenico and Schwartz, 1997). Advection (also known as convection) refers to heat transfer via moving groundwater (Domenico and Schwartz, 1997), and is commonly due to head gradients (Anderson, 2005). The volumetric heat capacity of water is greater than of geologic materials (Jury and Horton, 2004), and the thermal diffusivity (i.e., the ability to conduct heat relative to the ability to store heat) of water is low (Stonestrom and

Blasch, 2003). Thus, heat conduction is a slow process in saturated media. Heat transfer due to advection occurs faster than conduction where groundwater flows through saturated sediments (Hoffmann et al., 2003). Temperature profiles at depth are linear under static groundwater conditions, increasing with depth generally following the conduction-dominated geothermal gradient of 25 to 50 °C per kilometer (Anderson, 2005). Vertical advective flow is apparent in temperature profiles as deviations from the linear thermal gradients, indicating movement of groundwater from different depths (i.e., temperatures) (Anderson, 2005).

The analytical relationship between temperature and vertical groundwater flow was first realized in groundwater-surface water interfaces. Suzuki (1960) applied a transient heat-flow equation to determine infiltration based on shallow subsurface temperature variation. Stallman (1965) then developed an analytical model capable of estimating one-dimensional vertical velocity by simulating varying surface temperature profiles and groundwater temperatures in a column. The principles of inverse modeling (i.e., using observations to determine physical parameters) could also be applied to temperature and head measurements to calculate flow velocity at greater depths than the surface water interface (Stallman, 1963).

Bredehoeft and Papadopulos (1965) applied characteristics of temperature profiles in an analytical model to solve for vertical, time-independent groundwater flow in a well by using temperature data, type curves, and a relationship between advection and conduction. Later applications of the Bredehoeft and Papadopulos (1965) model applied the one-dimensional, constant temperature parameters to solve for aquifer-scale groundwater discharge (Cartwright, 1970; Taniguchi et al., 2003). Lu and Ge (1996) expanded the Bredehoeft and Papadopulos (1965) model to account for differences in vertical flow resulting from horizontal flow by allowing for calculation of flux in either dimension. Developments in temperature sensing

technology became catalysts for the widespread use of temperature data to characterize hydrogeologic flow systems.

Groundwater flow properties were characterized using heat as a tracer within boreholes (Leaf et al., 2012; Read et al., 2013; Banks et al., 2014; Sellwood et al., 2015) with an emerging technology known as distributed temperature sensing (DTS). Distributed temperature sensing returns temperature measurements at temporal and spatial scales that were previously unavailable and can provide unique opportunities for environmental monitoring (Selker et al., 2006; Tyler et al., 2009). Leaf et al. (2012) used DTS to measure borehole temperature as heated water was injected into a well complex and inferred fracture locations from measured vertical heat fluxes. Sellwood et al. (2015) showed similar estimates of borehole flow velocity between DTS heat-slug tracer tests and flowmeter results, which were within a range that overlapped previous flow measuring methods. Active heating methods showed promise to enhance groundwater flow identification in DTS deployments.

Distributed thermal perturbation sensing (DTPS) adds a continuous heating element in a DTS system to generate a temperature gradient. Freifeld et al. (2008) introduced this technique by applying constant heat (via current applied across a two-conductor cable) adjacent to the DTS cable to estimate the thermal conductivity of formations in a permafrost borehole. Read et al. (2014) deployed a DTPS system in a borehole under pumped conditions and found that differences in temperature profiles tracked closely with vertical velocities recorded by impeller tests. Banks et al. (2014) monitored temperature profiles of a DTPS system that was coiled to increase spatial resolution within a pumped open borehole and found that hydraulically active fractures were apparent in the temperature log as sharp reductions where cooler ambient groundwater flows into the borehole. Commonly, studies that use DTPS methods have only been

able to qualitatively assess groundwater flow, until Hausner et al. (2016) introduced a numerical model that quantifies flow in an aquifer using DTPS.

Previous Model: Quasi-One-Dimensional Radial Heat Transfer

Hausner et al. (2016) introduced a numerical model that relates radial heat transfer via conduction and advection with groundwater flow to quantify horizontal advection observed in a DTPS deployment. Hausner et al. (2016) first considered a conduction-only model (Figure 1A) that represents a section of blank well casing and simulates heat transfer into the surrounding media (Equations 1 through 4). The conduction-advection model (Figure 1B) adds advective heat fluxes to the conduction model, representing a section of screened casing where heat transfer is due to the combination of radial conduction and horizontal groundwater movement (Equation 5). Model approximated temperatures were then compared to observed temperatures to characterize model performance.

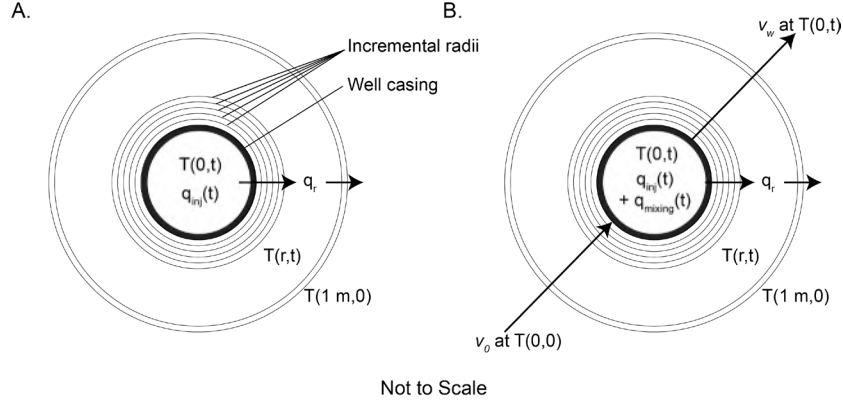


Figure 1: Numerical modeling approaches to radial heat transfer in a one-dimensional borehole cross-section. A: conduction-only model. B: conduction and advection model. Modified from Hausner et al. (2016).

Hausner et al. (2016) represents ideal radial heat transfer by:

$$q = -\lambda \frac{dT}{dr}, \quad (1)$$

where q represents heat flux (W/m^2), λ is thermal conductivity ($\text{W}/\text{K}/\text{m}$) and $\frac{dT}{dr}$ equals the thermal gradient (K/m). Hausner et al. (2016) used an energy balance to model temperature around the casing into the formation across incrementally increasing radii up to a distance of 1 m with:

$$\frac{dT_r}{dt} = \frac{q_{r1}2\pi r_1 h + q_{r2}2\pi r_2 h}{V C_v}, \quad (2)$$

where $\frac{dT_r}{dt}$ is the change in temperature over time (K/s) of incremental radii r_1 and r_2 (m), q_{r1} and q_{r2} are the heat fluxes through the inner and outer walls of each increment, respectively, h is the height (m), V is the volume (m^3), and C_v is the volumetric heat capacity ($\text{J}/\text{K}/\text{m}^3$) of the material. Hausner et al. (2016) combined Equations 1 and 2 and accounted for heat injection within the borehole as follows:

$$\frac{dT_b}{dt} = \frac{1}{V} \left(-D_T 2\pi r_1 h \frac{T_i - T_{i+1}}{\Delta r} + \frac{q_{inj}}{C_v} \right), \quad (3)$$

where $\frac{dT_b}{dt}$ equals the borehole temperature change over time, T_i is the temperature of an incremental cylinder (K), and q_{inj} is the heat injected from the cable heater (W/m), and D_T is the thermal diffusivity (m^2/s) of the formation. The thermal diffusivity is equal to the thermal conductivity divided by the heat capacity. The variable q_{inj} becomes zero when the period of heating concludes. Hausner et al. (2016) computed heat transfer into the formation with cylinders of incrementally increasing diameter:

$$\frac{dT_i}{dt} = \frac{1}{V} \left(-D_T 2\pi r_1 h \frac{T_i - T_{i-1}}{\Delta r} - D_T 2\pi r_2 h \frac{T_i - T_{i+1}}{\Delta r} \right), \quad (4)$$

where $\frac{dT_i}{dt}$ equals the change in temperature over time of an incremental cylinder i . Hausner et al. (2016) incorporated advective heat flux mixed with conduction in the combined conduction and advection equation:

$$\frac{dT_i}{dt} = \frac{1}{VC_v} \left[q_{inj} - \lambda \frac{T_i - T_{i+1}}{\Delta r} 2\pi r h \right] + \frac{v_0 2r h (T_0 - T_i)}{V}, \quad (5)$$

where $\frac{dT_i}{dt}$ equals the temperature over time of an incremental cylinder i , C_v is the heat capacity of water, v_0 is the Darcy velocity (m/s) (Darcy, 1856), r is the borehole radius, T_0 is the initial (i.e., background) temperature. The model assumed that the borehole fluid temperature was fully mixed, formation temperatures were isothermal at incremental radii, and formation temperature change was negligible 1 m away from the borehole.

Hausner et al. (2016) used observed borehole temperatures from a DTSPS deployment in observation wells under unstressed conditions and stressed conditions (i.e., when a nearby well was pumped). They modeled heat transfer (Equations 4 and 5) during heat injection and dissipation and optimized for horizontal groundwater flux based on the mass flux that minimized the error between observed and modeled borehole temperature. Hausner et al. (2016) identified

anisotropic hydraulic characteristics and zones with comparable flow rates to previous solute tracer tests in the alluvial aquifer, and they cited the need for numerical accounting of vertical flow to reduce the error associated with horizontal flow estimates. In this thesis, I build upon the existing quasi-one-dimensional radial groundwater and heat transfer numerical model (Hausner et al., 2016) to add vertical flow.

3. METHODS

I developed a two-dimensional radial coupled groundwater flow and heat transport model that considers vertical intra-borehole flow. Previous DTSP studies have not tested numerical models against synthetic data with known variables. I generated synthetic data sets to test model heat transfer assumptions, which included optimizing for formation thermal diffusivity. I then developed synthetic scenarios comprising prescribed variable flow fields and resulting borehole temperatures that were input into the two-dimensional model. I compared synthetic prescribed flux and temperature with model generated flux and temperature. I hypothesized that model generated flux is predictably similar to synthetically prescribed flux and that temperature is closely approximated by the model for various prescribed scenarios.

Two-Dimensional Radial Heat Transfer Model

The foundation for my study was the Hausner et al. (2016) one-dimensional numerical model that characterized the horizontal fluxes passing through the screened interval of a borehole based on temperature observations, the thermal properties of water, and the thermal properties of the formation. I added a second dimension to the existing model to consider heat transfer within sections of the borehole by its two component mechanisms:

1. Horizontal heat transfer through the screened interval. This mechanism included radial conduction away from the borehole and purely horizontal groundwater flow.
2. Vertical heat transport within the borehole. This mechanism assumed that intra-borehole vertical flow advected heat either upward or downward.

I discretized the borehole into cylinders every 12.5 cm, consistent with common DTS applications. The discretized elevation (depth) indices were linked together so the borehole resembled a single system, i.e., the vertical flux at the lower boundary of a shallow segment equaled the vertical flux at the upper boundary of a deeper, contiguous, segment. I evaluated horizontal radial conduction, influent advection, and effluent advection in combination with advection at upper and lower boundaries of the discretized segments to approximate temperature. I will refer to it as the “two-dimensional radial heat transfer model” for simplicity, although not all components are evaluated radially or in two dimensions.

The horizontal heat transfer equations (Equations 6 through 9) are based on Hausner et al. (2016) and I modified the equations in some cases. I describe the equations in this model in terms of energy balance at the control volume or a boundary. A discrete borehole cylinder is considered the control volume and the interface between the borehole and the formation or between the borehole cylinders is the boundary. Heat injection now includes a height scalar, h (m):

$$\frac{dE_{inj}}{dt} = q_{inj}h, (6)$$

where $\frac{dE_{inj}}{dt}$ is the change in energy over time (W) due to injected heat, q_{inj} , (W/m) and h (m) represents the height of the control volume. Heat injection was set to zero when the period of heating concluded. Radial conduction is:

$$\frac{dE_c}{dt} = q_{r1}2\pi r_1 h + q_{r2}2\pi r_2 h, (7)$$

where $\frac{dE_c}{dt}$ is the change in energy over time due to conductive heat flux (W/m²) through outward increments (q_{r1} and q_{r2}) of radii r_1 and r_2 (m), respectively, and h (m) is the height of the control volume.

I accounted for horizontal advection at each screened interval segment using Equations 8 through 13. Equation 8 represents advective heat flux entering the control volume:

$$\frac{dE_0}{dt} = v_0 r h \frac{\pi}{2} T_0 C_v, \quad (8)$$

where $\frac{dE_0}{dt}$ is the change in energy over time due to horizontal flow entering the control volume, v_0 is the inbound Darcy velocity (m/s) (Darcy, 1856), and T_0 is the ambient temperature of the formation. I assumed formation background temperature was constant at the initial temperature of the control volume. Equation 9 represents advective heat flux exiting the control volume:

$$\frac{dE_w}{dt} = v_w r h \frac{\pi}{2} T_b C_v, \quad (9)$$

where $\frac{dE_w}{dt}$ is the change in energy over time due to horizontal flow exiting the control volume, v_w is the outbound Darcy velocity (where v_w can be unequal to v_0), and T_b denotes the temperature of the borehole.

I added features to account for vertical advection in the mass and energy balance of the screened interval. Equations 10 through 13 considers advective heat transfer via vertical flow at the upper and lower boundaries of each discretized borehole segment. I resolved vertical advective heat transport at the upper boundary using Equation 10 for upward flow or Equation 11 for downward flow:

$$\frac{dE_{vu}}{dt} = -z_{up} \pi r^2 T_i C_v, \quad (10)$$

$$\frac{dE_{vu}}{dt} = -z_{up} \pi r^2 T_a C_v, \quad (11)$$

where $\frac{dE_{vu}}{dt}$ is the change in energy over time due to vertical flow at the upper boundary, z_{up} is the flow velocity at the upper boundary (m/s), where positive flow is upward, T_i (Equation 10) is the borehole temperature of the index increment, and T_a (Equation 11) is the borehole temperature of the above increment.

I resolved vertical advective heat transport at the lower boundary using Equation 12 for upward flow or Equation 13 for downward flow:

$$\frac{dE_{vl}}{dt} = z_{low}\pi r^2 T_{be} C_v, \quad (12)$$

$$\frac{dE_{vl}}{dt} = z_{low}\pi r^2 T_i C_v, \quad (13)$$

where $\frac{dE_{vl}}{dt}$ is the change in energy over time due to vertical flow at the lower boundary, z_{low} is the flow velocity at the lower boundary (m/s), where positive flow is upward, T_{be} (Equation 12) is the borehole temperature of the below increment, and T_i (Equation 13) is the borehole temperature of the index increment. The vertical velocity at a given boundary (e.g., upper) was not always equal to the vertical velocity at the opposite boundary (e.g., lower) of the same segment. I assumed vertical flow data were constant through the duration of the simulation. I set vertical flow to zero at the upper boundary of the top elevation index and at the lower boundary of the bottom elevation index.

I evaluated a total energy balance for each borehole segment considering the component energy fluxes of the control volume (Equation 14), and set a steady state mass balance (Equation 15) where inflows equaled outflows. The change in energy storage of the control volume is represented by temperature change (Equation 14) due to borehole heat injection (Equation 6), radial conduction (Equation 7), horizontal advection (Equations 8 and 9), and vertical advection (Equations 10 through 13). The combined energy balance is:

$$\frac{dT_b}{dt} = \frac{1}{VC_v} (E_{inj} - E_c + E_0 - E_w + E_{vu} + E_{vl}), \quad (14)$$

where $\frac{dT_b}{dt}$ is the change in borehole temperature over time, E_{inj} denotes energy injected by the cable heater, E_c is radial conduction, E_0 and E_w represents horizontal advection fluxes in and out of the control volume, respectively, E_{vu} denotes flux at the upper boundary, and E_{vl} corresponds

to flux at the lower boundary. Figure 2 shows the energy terms and functions used in the energy balance model. The model compared observed borehole temperatures against simulated borehole temperatures, then the horizontal flux variable, v_0 , was optimized to minimize the error between observed and simulated temperatures.

I combined Equations 8 through 11 into a volumetric mass balance of flow that considers model generated flux to solve for outbound Darcy velocity (v_w):

$$v_w = \frac{1}{\frac{\pi}{2}rh} (v_0 \frac{\pi}{2}rh - (z_{up} - z_{low})\pi r^2) , (15)$$

where v_0 equals the inbound Darcy velocity, z_{up} is the flow velocity at the upper boundary, and z_{low} is the flow velocity at the lower boundary. Figure 3 shows the terms and functions used in the heat transfer and mass balance model of discretized borehole cylinders.

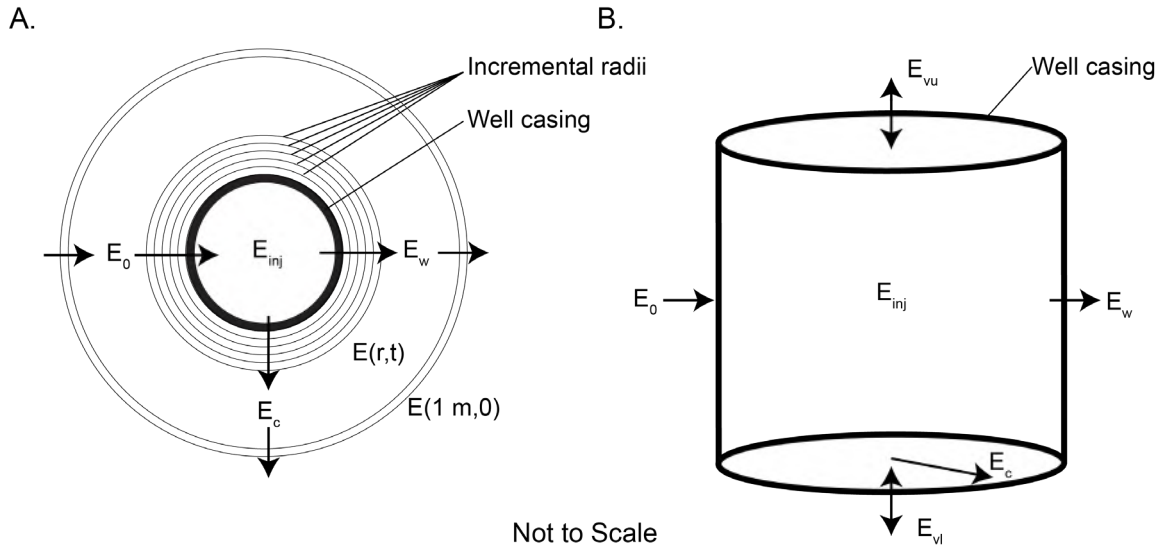
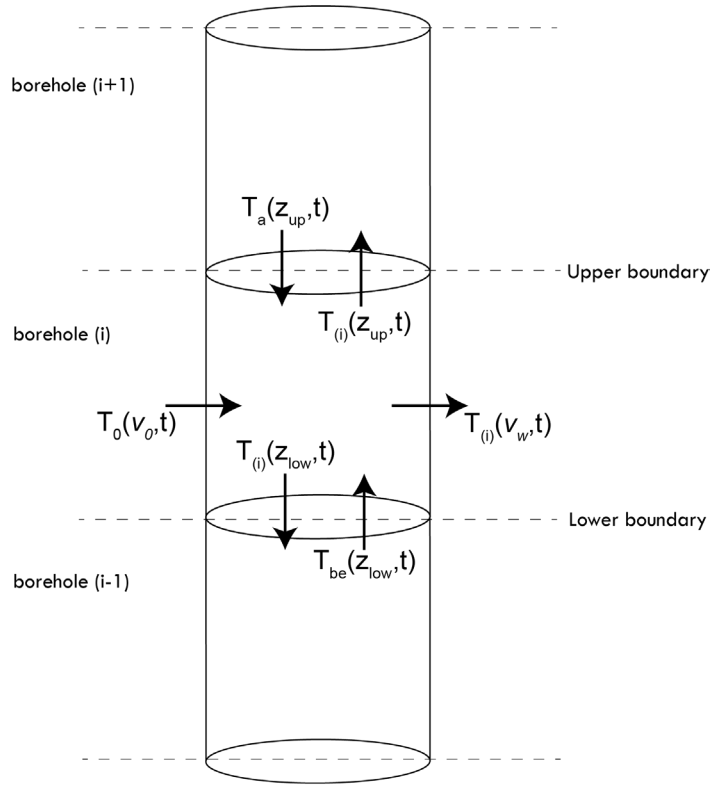


Figure 2: Energy terms used in numerical modeling. Where, A: radial heat transfer in a borehole cross-section, and B: combined vertical and radial heat transfer of a discrete borehole cylinder.



Not to Scale

Figure 3: Dynamic variables in the numerical modeling of discretized borehole cylinders. Shown at an elevation index of i .

Energy and mass balance (Equations 14 and 15, respectively) yielded a two-dimensional model of the screened section of the well that is discretized at representative intervals and dependent on intra-borehole flow interactions. I programmed the algorithms into MATLAB (MATLAB, 2019) with adjustable borehole geometry, heat capacity, heat injection, vertical flow, and formation thermal diffusivity. For all times, the model assumed that the borehole fluid temperature was fully mixed, formation temperature at an incremental radius was isothermal, and formation temperature change was negligible at 1 m away from the borehole, similar to the

Hausner et al. (2016) one-dimensional radial model. I chose MATLAB's ordinary differential equation (ODE) solver, *ode15s*, which requires an initial condition and an evaluation time span. The borehole temperature can be simulated throughout the screened interval and time series, based on customizable input assumptions and flows. In order to test the performance of the model, I produced various synthetic data sets consisting of variable flow fields and resulting temperatures.

Synthetic Data Set: Three-Dimensional Finite Element Analysis Model

Approach and Concept

I generated synthetic data sets using finite element analysis (FEA) to simulate changes in borehole temperatures in response to prescribed hydrogeologic flow settings. I generated synthetic data sets using FEATool, a MATLAB toolbox for modeling fully coupled systems of partial differential equations (PDEs) (Precise Simulation, 2020). It contains numerical solvers that couple systems of PDEs. This toolbox uses FEA to simulate complex systems in three-dimensions and is capable of simulating a downhole application with subdomains consisting of a borehole and formation. Additionally, FEATool enables model development and processing features relevant for model testing, including prescribed gradients (i.e., prescribed groundwater mass flux), user-defined functions for input variables, custom discretization at spatial intervals, and transient parameter evaluation at designated domain coordinates (Precise Simulation, 2020).

I developed the FEATool synthetic model based partly on a real-world DTSP application, reflecting the thermal and hydraulic properties of the formation as inferred in Hausner et al. (2016), but I prescribed hydraulic gradients to create different flow patterns for model evaluation. I selected equations that model fluid flow through a porous media and heat transfer

due to conduction and advection. I chose borehole geometry consistent with the screened interval of an observation well in Hausner et al. (2016). I prescribed physical properties for Darcian flow and heat transfer within the formation to represent an alluvial aquifer. Once the base model was complete, I varied the hydraulic boundary conditions and varied the formation hydraulic conductivity field. The flow rate and direction changed in response to prescribed conditions, resulting in unique advective heat transport scenarios.

Finite Element Model Development

I selected the FEATool pre-defined equations for Darcy fluid flow (Darcy, 1856) and heat transfer as the multiphysics modes (Equations 16 and 18, respectively). Darcy fluid flow takes the form:

$$d_{ts} \frac{\partial p}{\partial t} + \nabla \cdot \left(-\frac{\kappa}{\nu} \nabla p \right) = F, \quad (16)$$

where p equals pressure, t equals time, κ represents intrinsic permeability, ν equals kinematic viscosity, d_{ts} is a time scaling coefficient, and F accounts for a generated source or sink, such as a pump (Precise Simulation, 2020). Kinematic viscosity and intrinsic permeability are related to the hydraulic conductivity as shown in Equation 17 (Fetter, 2001):

$$K = \kappa \left(\frac{g}{\nu} \right), \quad (17)$$

where K is the hydraulic conductivity, κ represents intrinsic permeability, g is the acceleration due to gravity, and ν equals kinematic viscosity.

Heat transfer via conduction and advection takes the form:

$$\rho C_p \frac{\partial T}{\partial t} + \nabla \cdot (-k \nabla T) + \rho C_p u(x, y, z) \cdot \nabla T = Q, \quad (18)$$

where T equals temperature, t equals time, ρ is the density, C_p the heat capacity, k is the thermal conductivity, Q is the heat source term, and u is a vector valued advective velocity (i.e., the coupled flow velocity term in x , y , and z components) (Precise Simulation, 2020).

I generated the synthetic model domain composed of a cuboid with dimensions of $4 \times 2 \times 20$ m, (x , y , z , respectively) penetrated by a cylinder with a radius of 0.025 m and a height of 20 m. I produced a grid using a discretized polygon mean volume of 0.002 m^3 , resulting in 91,145 total polygons (i.e., cells). The cylinder and cuboid represented the open interval of the borehole and the surrounding aquifer formation subdomains, respectively. The borehole and formation subdomains had independent physical assumptions and interacted at internal boundaries with continuity conditions. The composite model domain consisted of the top boundary (i.e., top of the screen) at $z = 20$ m, the bottom boundary (i.e., bottom of the screen) at $z = 0$ m. I prescribed the hydraulic gradient horizontally with high to low head from $x = 0$ m to $x = 4$ m, therefore the upgradient and downgradient vertical boundaries were at $x = 0$ and $x = 4$ m, respectively. The hydraulic gradient was independent of the y -axis and varied in the z -axis according to my prescribed model scenarios.

In the saturated formation, the synthetic model assumed bulk subdomain properties (i.e., relative combination of fluid and solid matter). In the borehole, the synthetic model assumed pure water properties. Table 1 lists Darcy fluid flow constants used for synthetic advection models and Appendix A lists detailed justifications. I divided the formation subdomain into three horizontal sections that represent three homogenous and isotropic hydrostratigraphic units, each with a thickness of 7 to 8 m. The prescribed viscosity (and, by extension, hydraulic conductivity) is not temperature dependent due to the minimal differences in simulated temperature. I prescribed each unit a permeability that corresponds to a hydraulic conductivity in the range of

9.8e-5 to 7.4e-3 m/s (8.5 to 640 m/day), depending on the scenario. This range is consistent with the hydraulic properties of sand and gravel alluvial aquifers. I set a maximum hydraulic conductivity from Schwartz and Zhang (2003) in the borehole to allow effectively unobstructed flow within the borehole. I prescribed a hydraulic gradient of 1.4e-3 m/m, which is comparable to a representative regional hydraulic gradient in an alluvial aquifer (Hausner et al., 2016). I assigned a vertical head gradient one order of magnitude less than the horizontal gradient, and—depending on the scenario—the vertical gradient varied in direction and varied as a function of the z -axis.

Table 1: Darcy fluid flow assumptions used in the synthetic FEA model.

Parameter	Variable	Values	Source
borehole viscosity	ν	1.0e-6 m ² /s	(Fox et al., 2004)
borehole permeability	κ	1.0e-6 m ²	(Fetter, 2001)
borehole conductivity	K	1.0e-2 m/s	(Fetter, 2001)
bulk formation viscosity	ν	1.0e-6 m ² /s	(Fox et al., 2004)
bulk formation permeability	κ	1.0e-11, 1.0e-10, 5.0e-10, 7.5e-10 m ²	range applied from Belcher and Sweetkind (2010)
bulk formation conductivity	K	9.8e-5, 9.8e-4, 4.9e-3, 7.4e-3 m/s	range applied from Belcher and Sweetkind (2010)

Table 2 lists the heat transfer constants in synthetic advection models and Appendix A lists detailed justifications. I varied the formation thermal conductivity and heat capacity in synthetic simulations during the selection process of model thermal properties (described later in the “Thermal Diffusivity Model Scenarios” section), then I applied the best-fit values shown in Table 2 for all other synthetic advection models. I imposed a heating rate of 7.4 W/m, reflecting

the heating rate used in an actual DTSP deployment (Hausner et al., 2016). I set heat injection throughout the borehole subdomain volume, resulting in $3,817 \text{ W/m}^3$ injected during the first 500 minutes of simulation, then cooling was simulated for another 500 minutes. I assigned the model domain an initial thermal gradient of 0.007 K/m that increased linearly with depth, representative of an alluvial aquifer in Gillespie (2005). Most exterior boundaries assumed this gradient as a constant temperature condition, consistent with the assumption of steady-state background temperatures in the two-dimensional radial heat transfer model. I added three exceptions for model stability; the top and bottom boundaries of the borehole and the downgradient vertical formation boundary were instead a thermal outflow condition. I then coupled the borehole advective heat transfer to the component flow rate (Equation 18). Advective velocity was considered in the formation using the specific discharge vector components divided by porosity. In order to isolate the effect of advection due to fluid in the formation, I applied scalars to reconcile the bulk thermal properties of the saturated formation with separate properties for water and solid matter.

Table 2: Heat transfer assumptions used in the synthetic FEA model.

Parameter	Variable	Values	Source
borehole heat capacity	C_p	4,180 J/kgK	(Hausner et al., 2016)
borehole density	ρ	998 kg/m ³	(Fox et al., 2004)
borehole thermal conductivity	k	0.59 W/mK	(Jury and Horton, 2004)
borehole heat injection	Q	3,817 W/m ³	(Hausner et al., 2016)
formation heat capacity	C_p	1,647 J/kgK	Best-fit result
formation density	ρ	2,087 kg/m ³	(Fischer, 1992)
formation thermal conductivity	k	2.75 W/mK	(Robertson, 1988; Jury and Horton, 2004)
system temperature gradient	T	$294.007-(z)*0.007 \text{ K}$	(Gillespie, 2005)

I tested and verified models generated in FEATool to ensure the simulations were agreeable with the governing equations and that simulated processes occurred as expected. I applied each step toward a fully functional synthetic model individually then qualitatively monitored the flow and temperature characteristics as part of data quality assurance. Synthetic data scenarios (discussed later) were used as input into the two-dimensional radial heat transfer model.

Inverse Model Testing Approach

I tested the two-dimensional radial heat transfer model with given observations (i.e., the synthetic data) by inverting the time series of synthetic borehole temperature and optimizing for horizontal flux. Therefore, I refer to this heat transfer model with temperature inversion as the “inverse model”. Table 3 lists the inverse model assumptions, which are consistent with the synthetic data set where applicable. Additionally, I input synthetic vertical flow (where used) and synthetic borehole temperatures to the inverse model. I evaluated *ode15s* over the synthetic model time span (1,000 min) and assigned an initial condition for horizontal flux (v_0). Inverse model transient borehole temperatures are simulated and compared to synthetic temperature observations using the root mean square error (*RMSE*), shown in Equation 19. The model computes the *RMSE* of the time series at each elevation index using:

$$RMSE = \frac{1}{n} \sqrt{\sum_{i=1}^n (T - T_b)^2} , (19)$$

where n is the number of temperature observations, T is the synthetic borehole temperature and T_b denotes the inverse model borehole temperature. I optimized for horizontal flux using the MATLAB optimization routine *fminsearch*, which passed the v_0 value into the inverse model

then minimized the *RMSE* in an iterative process. The optimized inverse model wrote outputs for each elevation index and contained inbound horizontal mass flux of water (v_0) (referred to as “inverse flux”), the *RMSE*, and transient computed borehole temperature (T_b). The inverse model assumed inverse flux was constant, yet the advective heat flux was transient due to the variable temperature gradient between the initial formation and borehole temperatures. The inverse model required an appropriate thermal diffusivity that I determined.

Table 3: Constants and assumptions used in the inverse model.

Parameter	Variable	Value	Source
borehole radius	r	0.025 m	Consistent with synthetic data
borehole radius increment	Δr	0.001 m	Consistent with synthetic data
borehole height	h	0.125 m	Consistent with synthetic data
borehole volume	V	$2.45\text{e-}4 \text{ m}^3$	Consistent with synthetic data
heat injection	q_{inj}	7.4 J/s	Consistent with synthetic data
formation thermal diffusivity	D_T	$8.0\text{e-}7 \text{ m}^2/\text{s}$	Best-fit result
heat capacity of water	C_v	4,180 J/kgK	(Jury and Horton, 2004; Hausner et al., 2016)

Thermal Diffusivity Model Scenarios

I chose a best-fit thermal diffusivity by effectively varying the flow regime and formation heat transfer assumptions of synthetic models and corresponding inverse models. I compared the prescribed conditions to output from conduction-only inverse models and horizontal advection inverse models. I conducted a comparison of 12 conduction-only models assuming the six values of thermal diffusivity in Table 4 and evaluated the minimum *RMSE*. For the synthetic conduction models: (a) no hydraulic gradient was applied, (b) thermal conductivity ranged between

1.5 and 5.5 W/mK, and (c) heat capacity ranged between 1,317 and 1,916 J/kgK. I chose six of the 12 models for a comparison of horizontal advection. I applied a horizontal head gradient to induce flow in the synthetic model, and applied heat transfer constants corresponding to inverse model thermal diffusivities (Table 4). I based this evaluation on the error between prescribed (i.e., synthetic) and observed (i.e., inverse model) flow rates. After determining the best-fit thermal diffusivity, I generated the synthetic model scenarios that simulate vertical flow and variable aquifer conditions.

Table 4: Constants and assumptions used in the horizontal advection thermal diffusivity evaluation models.

Parameter	Variable	Values ^A	Source
inverse model: thermal diffusivity	D_T	5.0e-7, 8.0e-7, 9.0e-7, 1.0e-6, 1.3e-6, 1.6e-6 m ² /s	range applied between Jury and Horton (2004) and Hausner et al. (2016)
synthetic model: thermal conductivity	k	1.50, 2.75, 3.25, 3.50, 4.50, 5.50 W/mK	range applied between Robertson (1988) and Jury and Horton (2004)
synthetic model: heat capacity	C_p	1,437, 1,647, 1,730, 1,677, 1,725, 1,679 J/kgK	range applied based on selected thermal diffusivity

^AValues are listed in respective order, e.g., the inverse model that assumed $D_T = 5.0e-7$ m²/s corresponds to the prescribed synthetic model where $k = 1.5$ W/mK and $C_p = 1,437$ J/kgK.

Synthetic Model Scenarios with Variable Flow Fields

I prescribed synthetic model scenarios with variable flow fields and resulting borehole temperatures to use as observations in the inverse model. I effectively varied flow rates by assigning a hydraulic conductivity condition to individual hydrostratigraphic units. In addition to the horizontal hydraulic gradient, I imposed a vertical hydraulic gradient that resulted in either

upward or downward vertical flow. Table 5 lists the synthetic model scenarios and Figure 4 shows the hydraulic gradient and resulting flows for select types of model scenarios.

Scenario v1 has no vertical flow, and I varied the vertical gradient linearly as a function of elevation in v2. For scenarios v3 through v8, I applied the vertical gradient as a step function between the top and bottom units and varied it linearly as a function of elevation through the middle unit. In some cases, two model scenarios had similar structure, but with relatively higher or lower flow rates depending on the prescribed hydraulic conductivity. For example, I structured models v3 and v4 with downward vertical flow and a confining unit between aquifers. The prescribed hydraulic conductivities of units at a similar elevation were greater in model v3, resulting in relatively higher magnitude flows. The eight unique model scenarios were simulated for a given timespan.

I ran the synthetic model with an incremental time step of 3.3 minutes, resulting in 300 discrete times that comprise the 1,000 minute data series. I exported simulated average results along the borehole centerline with a vertical sampling interval of 0.125 m for temperature and vertical flow. I also evaluated the synthetic model generated horizontal specific discharge of the formation and refer to it as the “synthetic flux”. The synthetic formation seepage velocity—referred to as the “synthetic seepage velocity”—is equal to the synthetic flux divided by the porosity. Table 6 relates the assumed unit hydraulic conductivity to the synthetic flux and synthetic seepage velocity, which will be compared to inverse modeled flow rates. Exported vertical flow and temperature are input into the inverse model.

Table 5: Synthetic FEA model scenarios. The hydraulic conductivity condition is listed in order of elevation with the top (shallow) unit, the middle unit, and the bottom (deep) unit, in terms of the relative hydraulic conductivity listed in Table 6.

Model ID	Hydraulic conductivity condition	Description of model flow fields and hydrostratigraphic unit conditions
v1	low, mid, high	pure horizontal flow with variable unit hydraulic conductivity
v2	low	horizontal and downward vertical flow in a homogenous, isotropic domain
v3	high, low, high	high magnitude horizontal and downward vertical flow in a confining unit between aquifers
v4	mid, very low, mid	low magnitude horizontal and downward vertical flow in a confining unit between aquifers
v5	high, low, high	high magnitude horizontal and upward vertical flow in a confining unit between aquifers
v6	mid, very low, mid	low magnitude horizontal and upward vertical flow in a confining unit between aquifers
v7	very low, low, mid	low magnitude horizontal flow with variable unit hydraulic conductivity and upward flow in the middle elevation unit
v8	low, mid, high	high magnitude horizontal flow with variable unit hydraulic conductivity and upward flow in the middle elevation unit

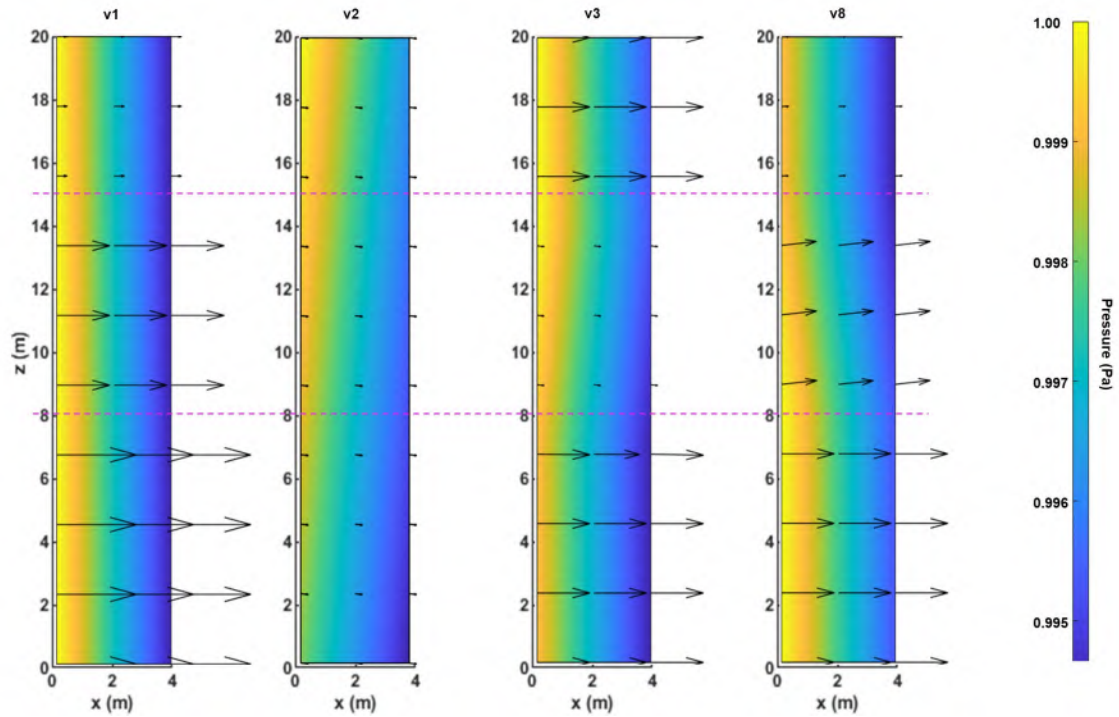


Figure 4: Plots of synthetic model flow scenarios. Shown in cross-section (x - z plane) of flow vectors (black arrows) and the pressure field (colored plot). From left to right: pure horizontal flow (v1), horizontal and vertical downward flow in a homogeneous domain (v2), and select cases of horizontal flow with vertical downward flow (v3) and vertical upward flow (v8). Contacts between units are shown as pink dashed lines.

Table 6: Synthetic FEA prescribed hydraulic conductivity, intrinsic permeability, formation flux, and formation seepage velocity.

Hydraulic conductivity condition	Hydraulic conductivity (m/s)	Intrinsic permeability (m^2)	Synthetic Flux (m/s; m/day)	Synthetic seepage velocity (m/s)
Very Low	$9.8e-5$	$1.0e-11$	$1.4e-7$; 0.01	$8.1e-7$
Low	$9.8e-4$	$1.0e-10$	$1.4e-6$; 0.12	$8.1e-6$
Mid	$4.9e-3$	$5.0e-10$	$6.9e-6$; 0.59	$4.0e-5$
High	$7.4e-3$	$7.5e-10$	$1.0e-5$; 0.89	$6.1e-5$

Temperature generated as part of the synthetic data set is taken as true for the purposes of assessing the inverse model's performance and will be referred to as "synthetic temperature". Temperature generated by the inverse model to approximate the synthetic temperature will be referred to as "inverse temperature". The mean temperature difference was calculated by taking the synthetic temperature minus the inverse temperature at each index and each timestep during the heating phase and during the cooling phase. To evaluate how inverse temperature reflected synthetic temperature, I quantified the hydrostratigraphic unit average temperature difference and *RMSE* for the eight model scenarios. To do this, the *RMSE* and temperature difference at each index were binned together according to hydrostratigraphic unit and averaged across the unit. This unit averaged *RMSE* and temperature difference will be referred to as "mean *RMSE*" and "mean temperature difference". The mean number of values (n) ranged between 26 and 55, depending on unit thickness. I neglected values within 1.0 m of unit contacts and of the top and bottom model boundaries to eliminate potential artifacts caused by contacts or boundary interfaces.

4. RESULTS

I present findings of comparisons between synthetic temperature and inverse temperature as well as between synthetic flux and inverse flux to: (a) identify the best-fit thermal diffusivity; (b) assess the inverse model accuracy of horizontal flow scenarios, in which the inverse model is similar in nature to the Hausner et al. (2016) model; and (c) assess the inverse model accuracy of horizontal and vertical flow scenarios, in which novel complexities are tested..

Thermal Diffusivity Evaluation

Table 7 shows the calculated flow rate error and the scenario averaged *RMSE* of model iterations computed at select indices across a subset of elevations in the model domain. The best-fit thermal diffusivity was $8.0e-7$ m²/s, which represents the minimum flow rate error between predicted and observed flow rate. Despite the minimal error, the conduction regime scenario averaged *RMSE* was occasionally lower with other thermal diffusivity assumptions, and the advection regime scenario average *RMSE* was commonly lower with other thermal diffusivity assumptions. Figure 5 shows synthetic and inverse temperature change for the conduction-only simulation using this thermal diffusivity. Inverse temperature was slightly underestimated during cooling compared to synthetic temperature but exhibited consistency in the shape and timing of heat transfer during heating (Figure 5). The pattern of synthetic temperature versus inverse temperature was highly variable with different thermal diffusivity values during heating. Commonly the timing and magnitude of temperatures were inconsistent and contrasted. Yet, the synthetic temperatures were always greater than inverse temperatures during the cooling phase.

Table 7: Mean flow rate error and scenario averaged *RMSE* for model iterations to determine the best-fit thermal diffusivity.

Thermal diffusivity (m ² /s)	Thermal conductivity (W/mK)	Heat capacity (J/kgK)	Mean flow rate error ^A	Conduction <i>RMSE</i> ^B (K)	Advection <i>RMSE</i> ^B (K)
5.0e-7	1.50	1,437	N/A	0.09	0.06
8.0e-7	2.75	1,647	-228%	0.05	0.04
9.0e-7	3.25	1,730	-381%	0.06	0.03
1.0e-6	3.50	1,677	-334%	0.05	0.03
1.3e-6	4.50	1,725	-447%	0.05	0.02
1.6e-6	5.50	1,679	-389%	0.03	0.02

N/A: Not applicable, calculated flow rate was zero.

^A Synthetic seepage velocity used as predicted flow rate, and inverse flux used as observed flow rate; $n=37$.

^B $n=21$.

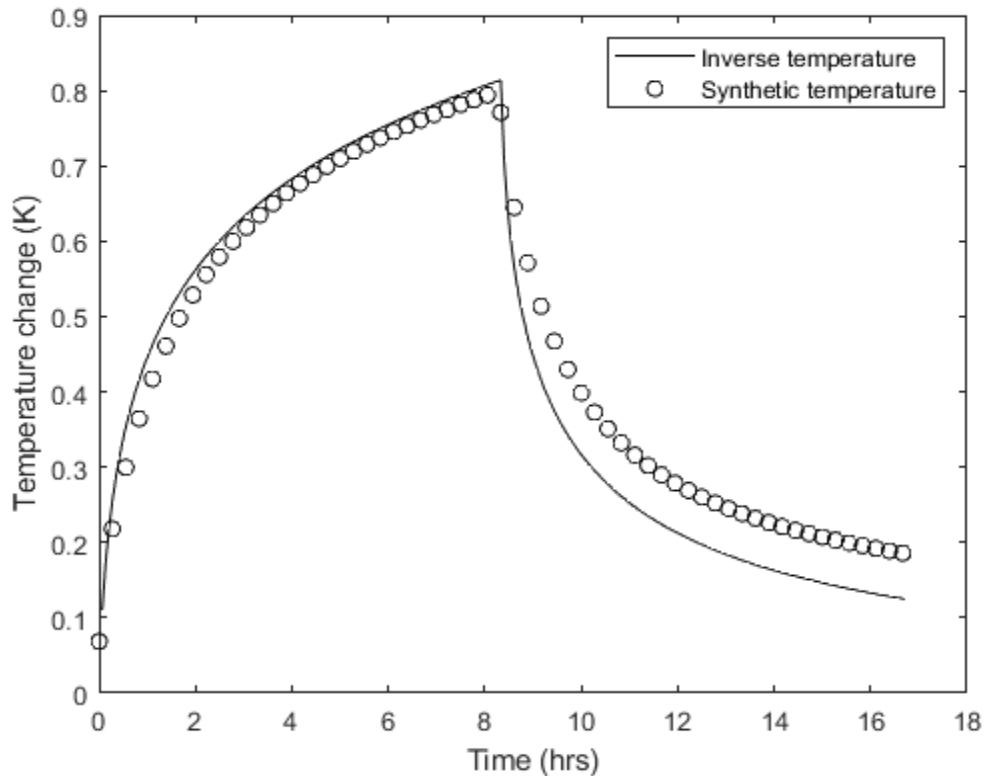


Figure 5: Temperature time series of model calculated heat transfer in a conduction-only regime. Shown at the midpoint elevation of the synthetic data set, assuming the best-fit thermal diffusivity. The scenario averaged *RMSE* is 0.05 K.

Horizontal Flow Scenario Comparison

Figure 6 shows synthetic model generated plots of the pure horizontal flow scenario (v1), including the pressure field, flow vectors, temperature time series, and cross-sectional temperatures. As expected, units with greater hydraulic conductivity corresponded to greater flow velocities, less borehole temperature change from background, and greater advective transport into the formation. Figure 7 shows the time series of synthetic and inverse temperatures in the horizontal flow scenario (v1) at elevations related to the three simulated hydrostratigraphic units with variable hydraulic conductivity. For each unit the inverse temperature underestimated the synthetic temperature during heating and overestimated it during cooling. The pattern and timing of the high and mid hydraulic conductivity realizations were different than those of the low hydraulic conductivity. The inverse temperature typically exhibited a gradual logarithmic profile at the onset of heating and cooling in contrast to the abrupt step-like change exhibited by the synthetic temperature.

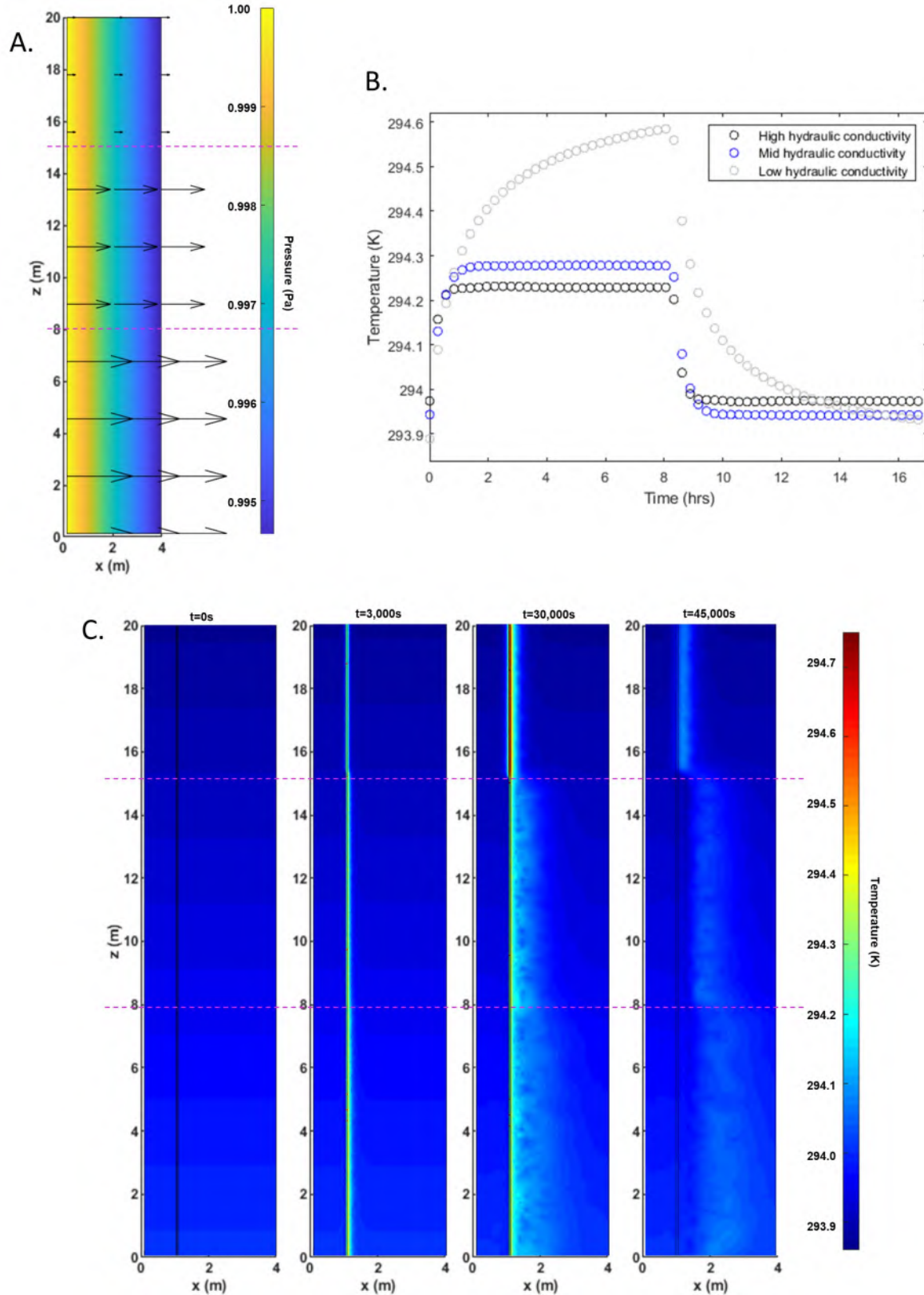


Figure 6: Synthetic model generated plots of the horizontal flow scenario (v1). A: cross-section (in the x - z plane) of flow vectors (black arrows) and the pressure field (colored plot).

B: temperature time series of model calculated heat transfer at representative elevations of the three simulated hydrostratigraphic units. C: cross-section (in the x - z plane) of temperature (colored plot) at time steps that correspond to background ($t = 0$ s), early heating ($t = 3,000$ s), end of heating ($t = 30,000$ s), and midway during cooling ($t = 45,000$ s). The borehole is located at $x = 1$ m and contacts between units are shown as pink dashed lines. Low hydraulic conductivity is the top unit ($z > 15$ m), mid hydraulic conductivity is the middle unit ($8 \text{ m} < z < 15 \text{ m}$), and high hydraulic conductivity is the lower unit ($z < 8$ m).

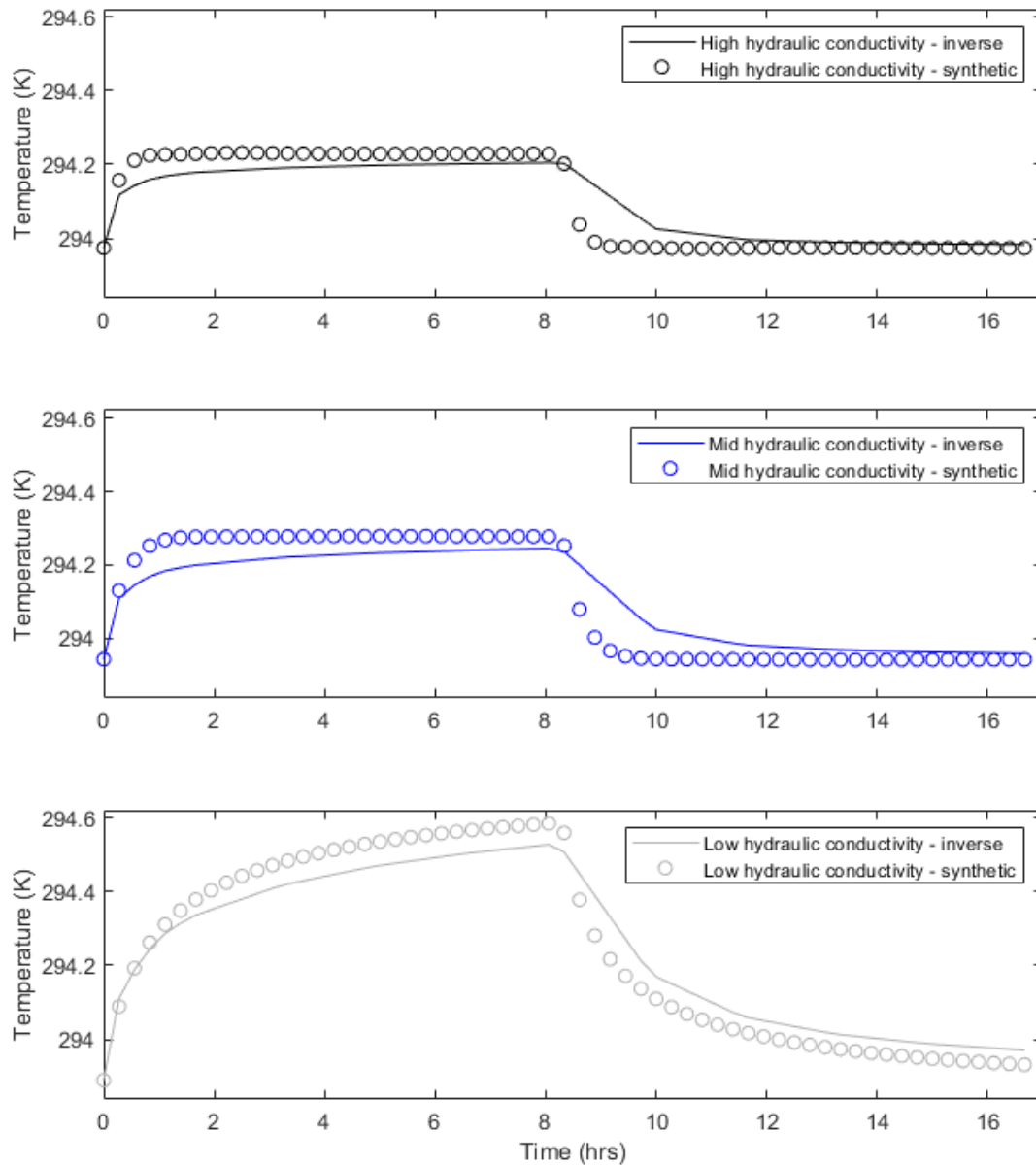


Figure 7: Temperature time series comparison of synthetic and inverse temperatures in the horizontal flow scenario (v1). Shown at representative elevations of the three simulated hydrostratigraphic units. The mean *RMSE* for the low, mid, and high hydraulic conductivity units is $3.31e-4$, $2.89e-4$, and $2.85e-4$ K, respectively.

Horizontal and Vertical Flow Scenarios Comparison

Simulations with vertical flow exhibited temperature profiles that were similar to profiles observed in the purely horizontal scenario (v1). Temperature curves for all scenarios with vertical flow are presented in Appendix B. These curves show that inverse temperature was consistent with synthetic temperature for very low hydraulic conductivity simulations only. The inverse temperature generally underestimated the synthetic temperature during heating and overestimated it during cooling at high, mid, and low hydraulic conductivities. The differences in profile at the onset of heating and cooling, i.e., the abrupt change of the synthetic temperature and the gradual change of the inverse temperature, are pronounced in the high and mid hydraulic conductivity realizations and not apparent in the low and very low hydraulic conductivity cases.

Table 8 presents the inverse flux as compared to synthetic flow rates for all model scenarios and hydrostratigraphic units. I calculated the mean inverse flux as the unit averaged flux and neglected values within 1.0 m of unit contacts and the top and bottom model boundaries. The unit averaged error between inverse flux and synthetic seepage velocity (or “mean flow rate error”) at the very low hydraulic conductivity condition was between 436% and 605% (mean = 549%, $n = 3$) and are considered unreliable. Generally, inverse flux overestimated the synthetic flux by about one order of magnitude. Inverse flux was greater than the synthetic seepage velocity by about a factor of two among the low, mid, and high hydraulic conductivities and across all scenarios. The inverse model predictably computed flow rate between 63% and 134% (mean = 93%, $n = 15$) greater than the prescribed seepage velocity. Figure 8 shows the inverse flux, the synthetic flux, and the synthetic seepage velocity across a range of hydraulic conductivities. Figure 9 shows the mean flow rate error associated with inverse flux of each scenario. As mentioned, the computed flux overestimated the prescribed flow rate, yet the

repeatability of these data—evidenced by the clustering of flow rate error at similar hydraulic conductivities in Figure 9—shows strong predictability of synthetic flow at low, mid, and high hydraulic conductivities.

Table 8: Computed inverse flux as compared to prescribed synthetic flow rates. Shown for all model scenarios and hydraulic conductivities.

Model version	Hydraulic conductivity condition	Synthetic flux (m/s)	Synthetic seepage velocity (m/s)	Mean inverse flux ^B (m/s)	Mean inverse flux standard deviation ^B (m/s)	Mean flow rate error ^A (%)
v1	Low	1.37e-6	8.08e-6	1.52e-5	9.67e-7	88.1
	Mid	6.87e-6	4.04e-5	9.46e-5	5.52e-6	134
	High	1.03e-5	6.06e-5	1.38e-4	7.89e-6	129
v2	Low	1.37e-6	8.08e-6	1.48e-5	1.34e-6	83.2
v3	Low ^C	1.37e-6	8.08e-6	1.49e-5	1.26e-6	84.4
	High	1.03e-5	6.06e-5	1.14e-4	7.63e-6	88.9
v4	Very low ^C	1.37e-7	8.08e-7	5.70e-6	9.34e-7	606
	Mid	6.87e-6	4.04e-5	7.96e-5	3.99e-6	97.0
v5	Low ^C	1.37e-6	8.08e-6	1.61e-5	1.25e-6	99.3
	High	1.03e-5	6.06e-5	1.15e-4	7.65e-6	89.0
v6	Very low ^C	1.37e-7	8.08e-7	5.70e-6	8.91e-7	606
	Mid	6.87e-6	4.04e-5	7.97e-5	3.91e-6	97.3
v7	Very low	1.37e-7	8.08e-7	4.33e-6	7.78e-7	436
	Low	1.37e-6	8.08e-6	1.38e-5	1.30e-6	70.8
	Mid	6.87e-6	4.04e-5	7.79e-5	3.88e-6	92.8
v8	Low	1.37e-6	8.08e-6	1.32e-5	9.48e-7	63.4
	Mid	6.87e-6	4.04e-5	7.80e-5	5.50e-6	93.1
	High	1.03e-5	6.06e-5	1.14e-4	7.43e-6	88.8

^A Formation seepage velocity used as predicted flow rate, and inverse flux used as observed flow rate; n ranges between 26 and 55, depending on unit thickness.

^B n ranges between 26 and 55, depending on unit thickness.

^C Values are averaged using the top and bottom units of similar hydraulic conductivity; $n=2$.

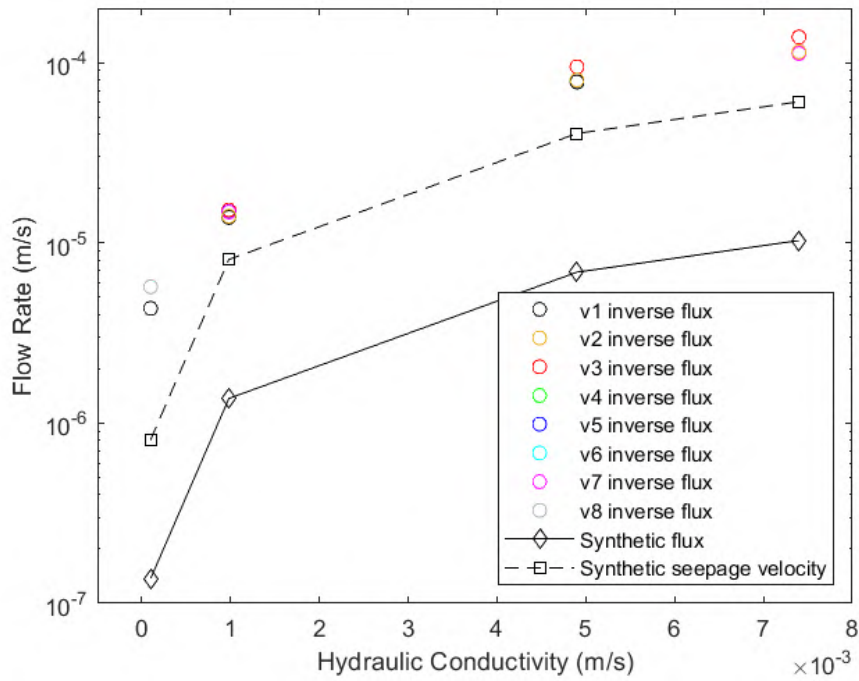


Figure 8: Computed inverse flux and prescribed synthetic flux and seepage velocity at various hydraulic conductivities.

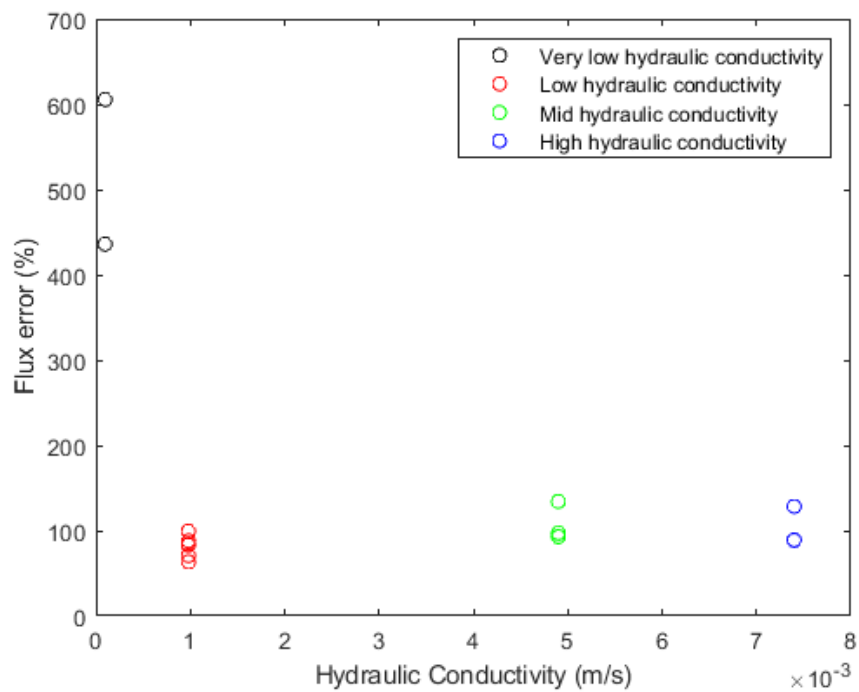


Figure 9: Mean flow rate error associated with computed inverse flux and prescribed synthetic seepage velocity at various hydraulic conductivities.

5. DISCUSSION

I characterize errors and limitations of the inverse and synthetic models by considering a dissimilarity in modeling physics and through further comparisons of flux and temperature. I explain the resulting biases, which are addressed in a detailed analysis of temperature differences between modeled and expected temperature. I discuss this study's observed flow rate limits and how they pertain to the theoretical calculable limits, then suggest improvements to inform users who may apply this modeling approach.

Systematic Error Due to Modeling Mechanics

A systematic error that biased all temperature comparisons between the two models is likely attributed to a difference in the mechanics of advective heat transfer between the synthetic and inverse models. Conductive heat transfer moved injected heat radially outward in all directions from the borehole in both the synthetic and inverse models. Horizontal advected heat transfer in the synthetic model moved heat into the borehole at the upstream temperature surrounding the borehole. By contrast, horizontal advection in the inverse model moved heat into the borehole at the initial, cooler, background temperature. Near the upstream edge of the borehole in the synthetic model, horizontal advection counters components of conduction to an unknown degree. However, in the inverse model, heat dissipates by the cumulative effects of conduction and advection, which are independent of direction. Therefore, heat dissipates faster in the inverse model where comparatively cooler borehole temperature is present, despite theoretically equal advective flow rates. I believe that inverse flux is biased greater than synthetic flux because warmer temperature that persists in the synthetic data during heat injection (Figure 7) does not dissipate as assumed in the inverse model. Inverse flux

consequently increases to compensate for the warmer synthetic temperature. Model performance and the systematic error between synthetic and inverse temperature can be better understood by considering the temperature difference during heating and cooling phases for each model scenario.

Temperature Comparison of Model Scenarios

Figure 10 presents the mean temperature difference between synthetic temperature and inverse temperature for hydrostratigraphic units and heating/cooling phases among the eight model scenarios. The variability in the mean temperature difference is generally low between similar units and between the heating and cooling phases within similar units (Figure 10). Models that include vertical flow exhibit very low variability among similar units. Mid and high hydraulic conductivities in the horizontal flow scenario (v1) exhibit a slightly lower mean temperature difference when compared to the hydraulic conductivities of other scenarios. Standard deviations (error bars in Figure 10) are greater during the cooling phase for most model scenarios and units. This is due to the difference between synthetic and inverse temperature observed during the cooling phase of the conduction-only model (Figure 5).

I then averaged the difference between the synthetic and inverse temperature and the *RMSE* for each unit across all model scenarios (Table 9). The scenario averaged temperature difference is greater for low and mid hydraulic conductivities, indicating that units which were neither conduction-dominated (i.e., very low hydraulic conductivity) nor advection-dominated (i.e., high hydraulic conductivity) did not approximate temperatures as accurately. The systematic error due to modeling mechanics is therefore less prevalent in scenarios that are dominated by one mechanism of heat transfer, where the relative contribution from the other mechanism is minimal. For example, the temperature difference is relatively low for the

advection-dominated condition (high hydraulic conductivity in Figure 10 and Table 9) because conductive heat transfer is negligibly small. In this case, the systematic error between synthetic and inverse models is limited, resulting in more agreeable simulated temperatures. The systematic temperature difference error is not correlated to the mean flow rate error or the mean *RMSE*. The inverse flux of the very low hydraulic conductivity condition exhibited the highest mean flow rate error, the lowest scenario averaged temperature differences, and the highest scenario averaged *RMSE*. The relatively high flow rate error associated with very low hydraulic conductivities indicates that this modeling approach has a limited range of calculable flux, and that the inverse flux determined in the conduction-dominated regime is less than the lower limit.

The systematic error due to modeling mechanics has consistent effects on the temperature and flux comparisons between synthetic and inverse models. Temperature differences are highly consistent among similar units (Figure 10), and the inverse flux constantly overestimated synthetic seepage velocity in the low, mid, and high hydraulic conductivity units (Table 9). Given the physical nature of this error and the consistent effects, I am confident that inverse model results are qualitatively accurate representations of the prescribed conditions. I assert that the inverse model reliably optimized flux between $1.4\text{e-}6$ m/s (0.12 m/day) and $1.0\text{e-}5$ m/s (0.89 m/day) in a variety of flow scenarios. Therefore, it may be appropriate to scale the inverse flux to the synthetic flux to correct for the systematic error.

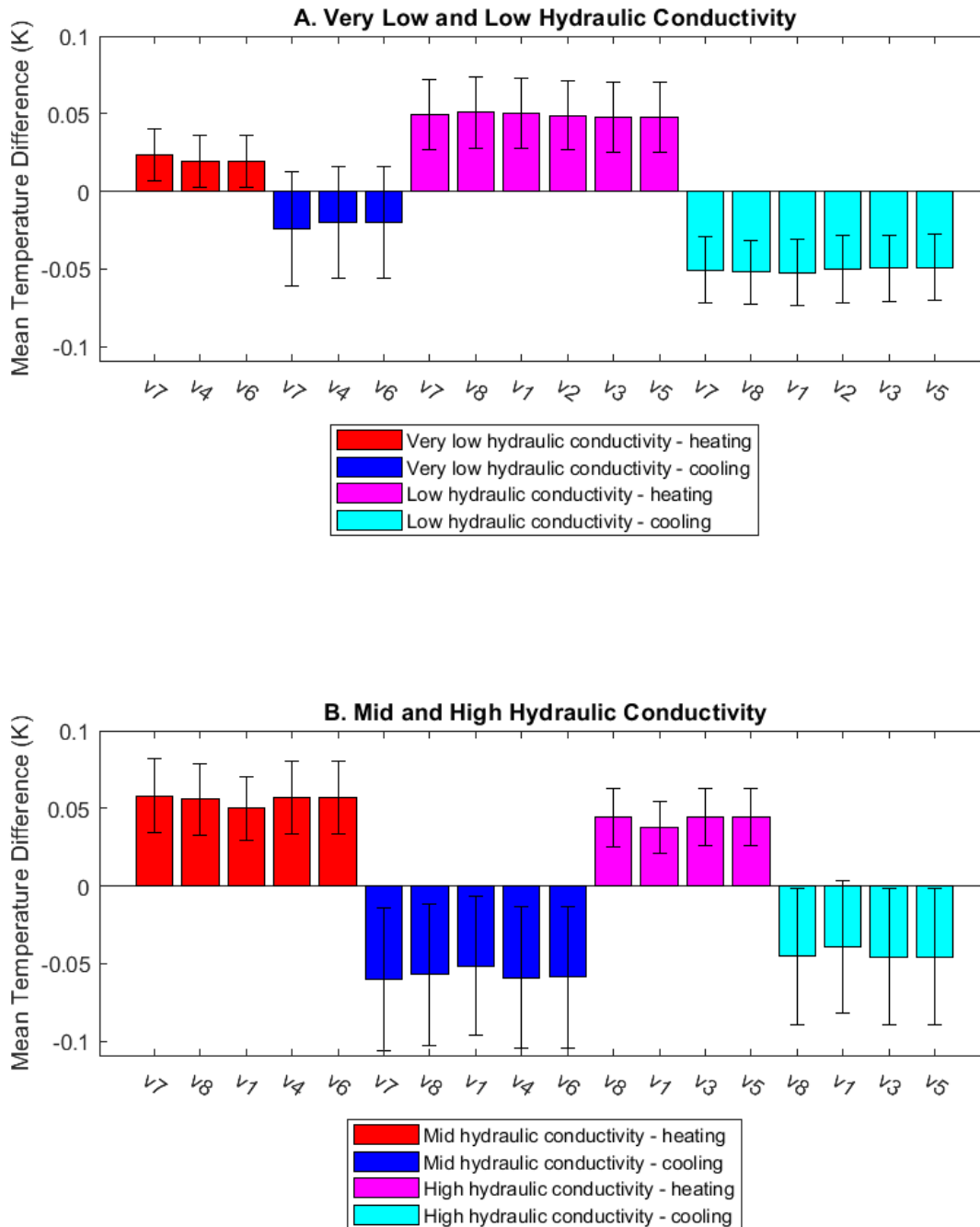


Figure 10: Mean temperature difference between prescribed synthetic temperature and computed inverse temperature for all eight model scenarios. Where, A: very low and low hydraulic conductivity units and, B: mid and high hydraulic conductivity units. Error bars represent the standard deviation. Mean n ranges between 26 and 55, depending on unit thickness.

Table 9: Scenario averaged temperature difference and *RMSE* between synthetic and inverse temperatures.

Hydraulic conductivity	Heating: temperature difference ^A (K)	Cooling: temperature difference ^A (K)	<i>RMSE</i> ^A (K)
High ^B	4.25e-2 ± 1.81e-2	-4.39e-2 ± 4.37e-2	2.84e-4 ± 4.14e-4
Mid ^C	5.55e-2 ± 2.27e-2	-5.73e-2 ± 4.54e-2	3.06e-4 ± 6.39e-4
Low ^D	4.90e-2 ± 2.27e-2	-5.07e-2 ± 2.12e-2	2.93e-4 ± 4.69e-4
Very Low ^E	2.06e-2 ± 1.70e-2	-2.15e-2 ± 3.64e-2	3.39e-4 ± 7.37e-4

^A Mean *n* ranges between 26 and 55, depending on unit thickness.

^B Values are averaged across all scenarios, *n* = 4.

^C Values are averaged across all scenarios, *n* = 5.

^D Values are averaged across all scenarios, *n* = 6.

^E Values are averaged across all scenarios, *n* = 3.

Calculable Flow Rate Limits

I prescribed a range of synthetic flux between 1.4e-7 m/s (0.01 m/day) and 1.0e-5 m/s (0.89 m/day), however, this does not represent the range of reliably calculated Darcy flux. The inverse flux at very low hydraulic conductivity was significantly greater than the prescribed synthetic seepage velocity (by about a factor of five) (Table 8). This suggests the inverse model cannot reliably predict flow rate in the conduction-dominated regime, and the minimum calculable synthetic flux is 1.4e-6 m/s (0.12 m/day). The maximum synthetic flux of 1.0e-5 m/s (0.89 m/day) is imposed by the synthetic model, where flux greater than 1.0e-5 m/s (0.89 m/day) resulted in numerical instability in the model. Numerical instability of the flow field manifested as unreasonable velocity vectors that propagated through the synthetic model domain. These velocity magnitudes were out of the anticipated range (by many orders of magnitude) and flow vectors unexpectedly changed direction in subsequent time steps. Temperature instability was expressed as surges, in which borehole temperatures exhibited artificial peaks and troughs in

presumed steady-state temperature conditions. Model troubleshooting involved reducing the grid size, increasing the time step, and decreasing the hydraulic and temperature gradients, but was unable to reduce instability. Therefore, the solvable range of prescribed Darcy flux in my study is between $1.4\text{e-}6$ m/s (0.12 m/day) and $1.0\text{e-}5$ m/s (0.89 m/day).

Hatch et al. (2006) and Glose et al. (2019) researched the limits where Darcy flux is reliably calculated using heat as a tracer. They considered the deflection of conductive heat transfer due to advective heat transfer where discharge occurs at groundwater-surface water interfaces. Although the hydrologic settings of those studies were not boreholes, the principles of heat transfer through porous media are widely applicable and are relevant here. Hatch et al. (2006) found that Darcy flux could be reliably determined up to $3\text{e-}5$ m/s (3 m/day), which is greater than my range of prescribed flux. This upper limit—found through simulating synthetic streambed data—is rarely exceeded in nature and numerous studies have confirmed the maximum detectable flux (Briggs et al., 2014; Briggs et al., 2012; Goto et al., 2005; Irvine et al., 2015). Glose et al. (2019) simulated synthetic thermal conditions in saturated sediment for a range of temperature sensor resolutions, thermal diffusivities, and the relationship between conduction and advection. Glose et al. (2019) determined the minimum calculable Darcy flux of $1\text{e-}7$ m/s (0.01 m/day), which is comparable to my conduction-dominated synthetic flux condition. Given the range of theoretically solvable Darcy flux, I assume the inverse model is capable of optimizing for higher flux and attribute the limitation to the synthetic FEA solver.

Potential Improvements to the Model Approach

The assumptions applied to the inverse model could be improved in future developments to minimize errors. The conduction-only synthetic and inverse modeled temperatures exhibited a consistent shape across different values of thermal diffusivity. The synthetic temperatures were

greater than inverse temperatures during the cooling phase, such as in Figure 5. This error points to an inherent bias between the synthetic and inverse models, which I suspect is due to a difference in heat transport among elementally discretized nodes in three dimensions. The systematic error due to model mechanics can be addressed in the inverse model by re-evaluating heat transfer components immediately upstream of the borehole. Improvements would consider formation temperature and add directionality that accounts for the competing influence of conduction and advection. These improvements require transitioning the inverse model from the two-dimensional radial approach to a three-dimensional simulation. A three-dimensional model would demand substantially greater computational resources—especially considering the inverted optimization process that requires repetitive solving—and is outside the scope of this thesis.

In addition to the identified systematic errors, another potential source of error may affect the model comparisons. In the synthetic model, flow paths near the interface of the borehole and formation are slightly deflected towards the borehole despite no prescribed flow in the y -direction due to the higher hydraulic conductivity of the borehole. The inverse model neglects flow path deflection, which introduces some uncertainty to inverse model comparisons. I expect that flow convergence at the center of the borehole would lead to higher flow through the center and faster dissipation of heat. I attempted to simulate a condition where flow convergence is neglected, however FEATool does not support enforcing a flow constraint (i.e., setting flow in the y -direction to zero) or fixing a coefficient pointwise in domains. I compared synthetic models where advective heat transfer was uncoupled in the y -direction to the original (i.e., coupled) models, but the findings of borehole temperature differences were ambiguous. This issue requires a separate investigation to empirically evaluate a scenario where flow convergence is

neglected. Flow path convergence may be more pronounced in applications with higher flow rates, large diameter boreholes, and sizable annular space.

The synthetic and inverse models do not consider the complexities of a field DTS deployment, particularly those associated with well construction. Hydraulic and heat transfer processes are complicated by installed materials such as the slot geometry of a screen, the thermal properties of these materials, and the porosity and hydraulic conductivity of a gravel pack, among others. Well construction complexities did not contribute to errors in my study because the boreholes in the inverse and synthetic models are completely open to the formation. However, well construction characteristics should be considered if this modeling approach is applied to field deployments.

6. CONCLUSION

The results from the inverse model are encouraging because prescribed synthetic flux and borehole temperature was reliably approximated, except where synthetic flux was outside of the calculable flow rate limits. Model predictions were affected by a systematic error due to modeling mechanics, which biased inverse flux and may have limited the range of reliable flux calculations. Potential improvements to the inverse model could be developed to address errors or to better represent field applications in future developments. The predictability of inverse flux and the consistency of temperature comparisons between the inverse and synthetic models are also promising, especially given the complexities incorporated in the flow regimes. My thesis addresses a deficiency in the quantification of groundwater flow using borehole temperature and highlights the importance of vertical flow observations to better simulate hydrogeologic systems. Further, my findings support the use of synthetic data in the testing and verification of numerical models, particularly when identifying limits or discerning the factors that contribute to errors.

APPENDIX A: Details of model assumptions used for synthetic advection models.

Table 10: Darcy fluid flow assumptions and justifications used in the synthetic FEA model.

Parameter	Variable	Values	Note
borehole viscosity	ν	1.0e-6 m ² /s	Kinematic viscosity of water at 20°C; Table A.8 in Fox et al. (2004).
borehole permeability	κ	1.0e-6 m ²	Intrinsic permeability determined by hydraulic conductivity corresponding to maximum material conductivity; Table 3.7 in Fetter (2001).
borehole conductivity	K	1.0e-2 m/s	Hydraulic conductivity corresponding to maximum material conductivity; Table 3.7 in Fetter (2001).
bulk formation viscosity	ν	1.0e-6 m ² /s	Kinematic viscosity of water at 20°C; Table A.8 in Fox et al. (2004).
bulk formation permeability	κ	1.0e-11, 1.0e-10, 5.0e-10, 7.5e-10 m ²	Intrinsic permeability determined by hydraulic conductivity range applied from Belcher and Sweetkind (2010) ^A .
bulk formation conductivity	K	9.8e-5, 9.8e-4, 4.9e-3, 7.4e-3 m/s	Hydraulic conductivity range applied from Belcher and Sweetkind (2010) ^A .

^A The hydraulic conductivity of a representative alluvial aquifer in Nevada ranges between from 5e-8 to 5e-3 m/s; geometric mean = 1.7e-5 m/s; and arithmetic mean = 1.3e-4 m/s (Belcher and Sweetkind, 2010).

Table 11: Heat transfer assumptions and justification used in the synthetic FEA model.

Parameter	Variable	Values	Source
borehole heat capacity	C_p	4,180 J/kgK	Heat capacity of water at 25°C (Hausner et al., 2016).
borehole density	ρ	998 kg/m ³	Density of water at 20°C; Table A.8 in Fox et al. (2004).
borehole thermal conductivity	k	0.59 W/mK	Thermal conductivity of water (Jury and Horton, 2004).
borehole heat injection	Q	3,817 W/m ³	Heat injection of 7.4 W/m in a representative DTSP deployment (Hausner et al., 2016); rate is divided by the borehole cylinder volume.
formation borehole heat capacity	C_p	1,647 J/kgK	Best-fit result based on the thermal diffusivity evaluation.
formation density	ρ	2,087 kg/m ³	Saturated density of a representative alluvial aquifer with sand and gravel; Table 2 in Fischer (1992) ^A .
formation thermal conductivity	k	2.75 W/mK	Thermal conductivity of a saturated sediment formation with porosity = 0.17 and quartz content between 20% - 30%, using Figure 10 in Robertson (1988). Consistent with thermal conductivity of saturated sandy soil Figure 5.11 in Jury and Horton (2004).
system temperature gradient	T	294.007-(z)*0.007 K	Temperature gradient of a representative alluvial aquifer where the gradient is equal to -0.007 K/m (Gillespie, 2005) in the vertical (z) direction.

^A Assuming a mean grain density (ρ_g) of 2.31 g/cm³ (Fischer, 1992), density of water (ρ_w) at 20°C = 0.998 g/cm³ (Fox et al., 2004), and porosity (n) = 0.17 (Hausner et al., 2016). Where saturated density (ρ_s) = $\rho_g(1-n) + \rho_w(n)$.

APPENDIX B: Temperature comparison curves of models that include vertical flow.

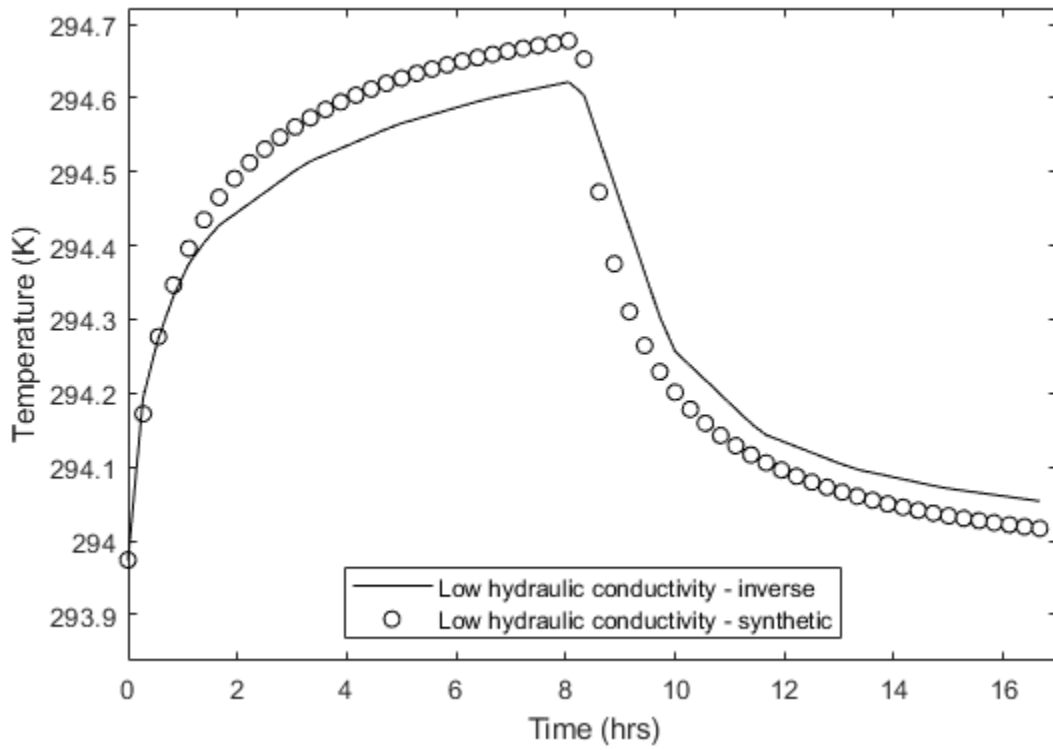


Figure 11: Temperature time series of model calculated heat transfer in model scenario v2. Shown at a representative elevation. The mean *RMSE* is $2.93e-4$ K.

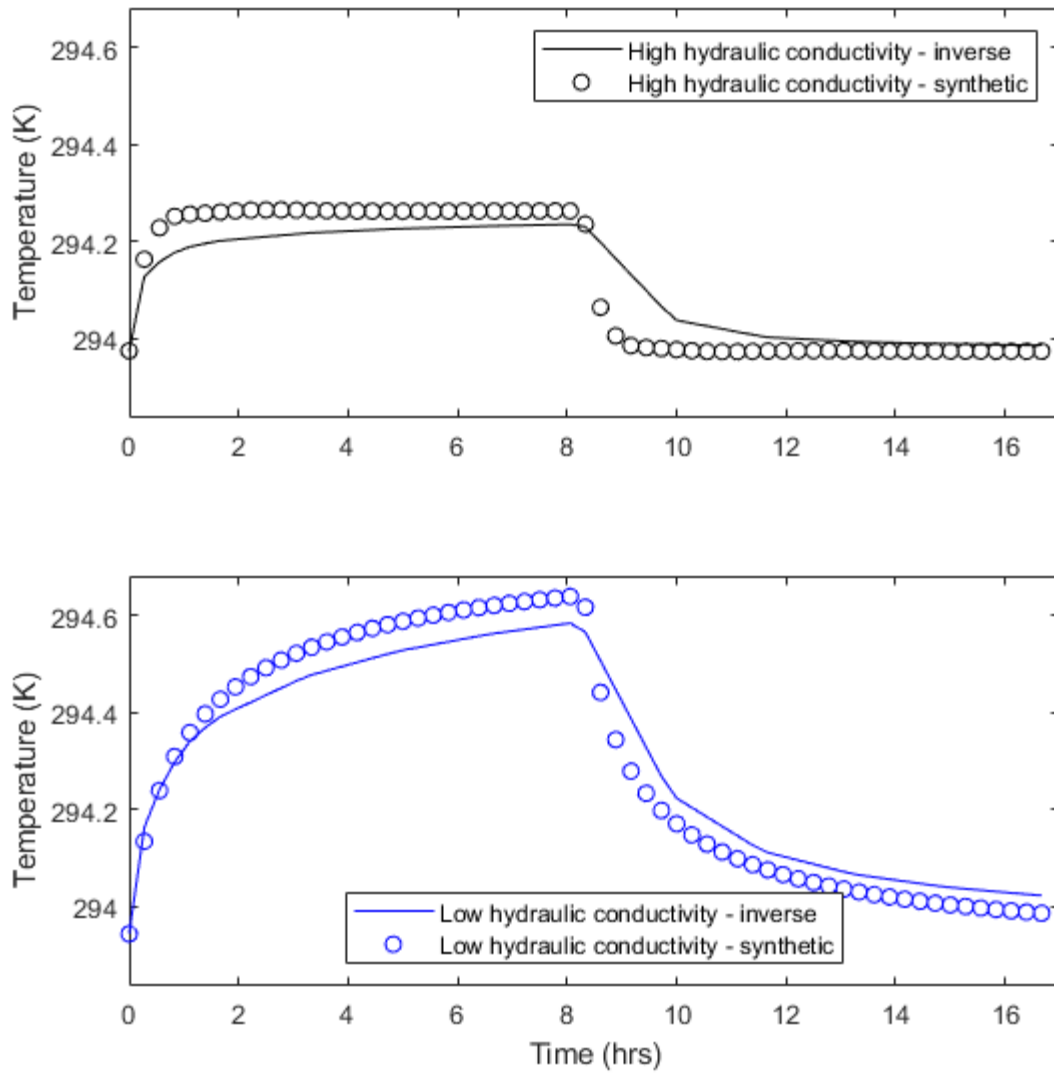


Figure 12: Temperature time series of model calculated heat transfer in model scenario v3. Shown at representative elevations of the simulated hydrostratigraphic units. The mean *RMSE* for the low and high hydraulic conductivity units is $2.45e-4$ and $2.88e-4$ K, respectively.

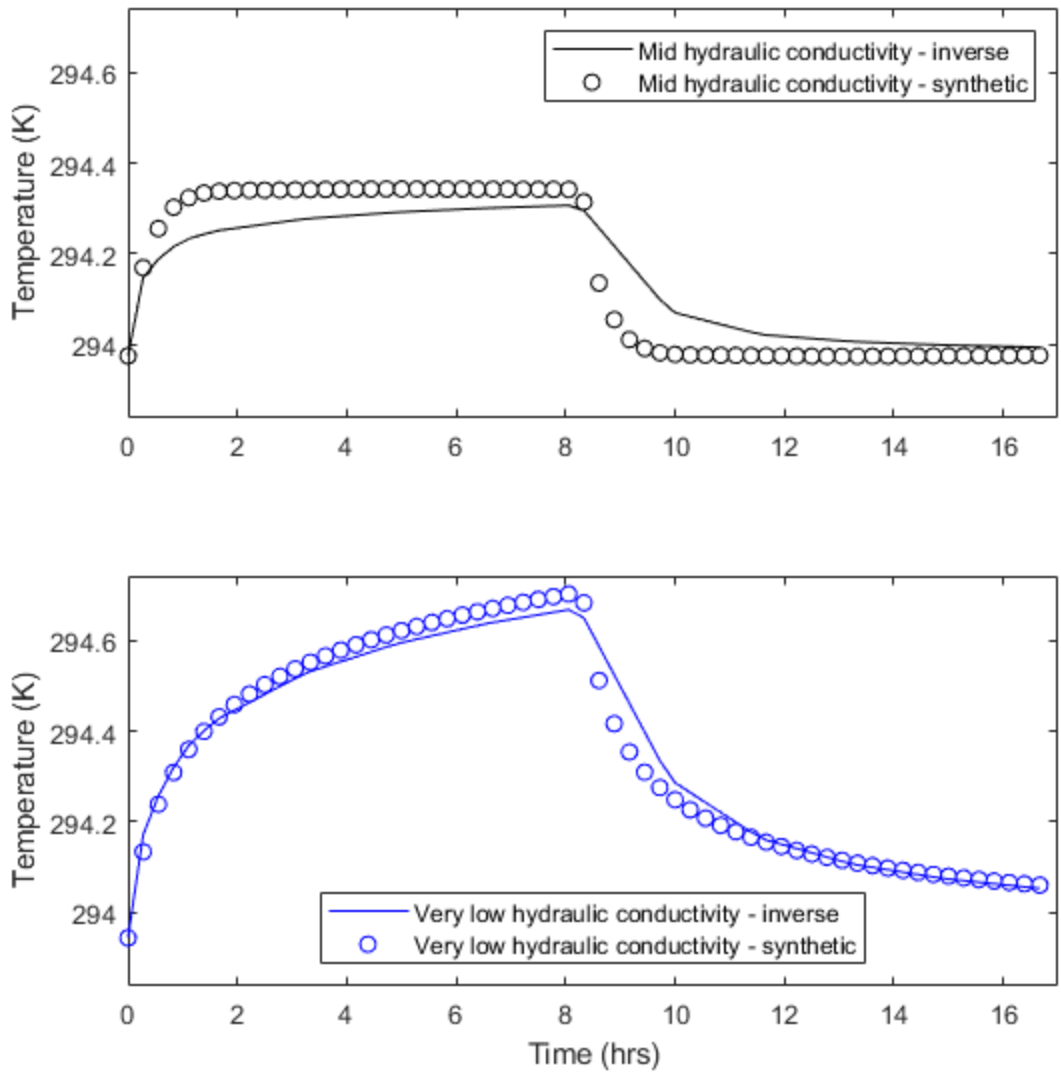


Figure 13: Temperature time series of model calculated heat transfer in model scenario v4. Shown at representative elevations of the simulated hydrostratigraphic units. The mean *RMSE* for the very low and mid hydraulic conductivity units is $2.95e-4$ and $2.31e-4$ K, respectively.

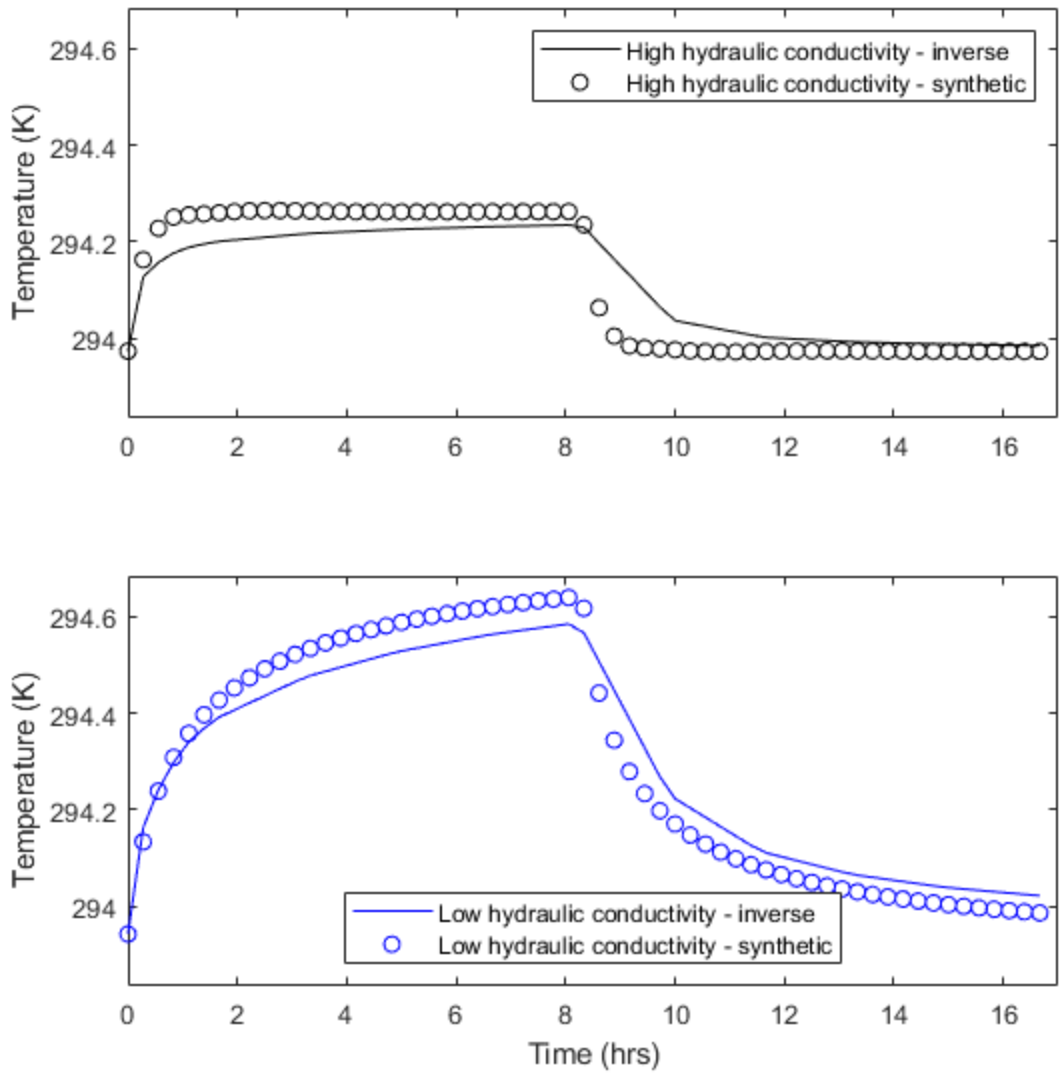


Figure 14: Temperature time series of model calculated heat transfer in model scenario v5. Shown at representative elevations of the simulated hydrostratigraphic units. The mean *RMSE* for the low and high hydraulic conductivity units is $2.71e-4$ and $3.71e-4$ K, respectively.

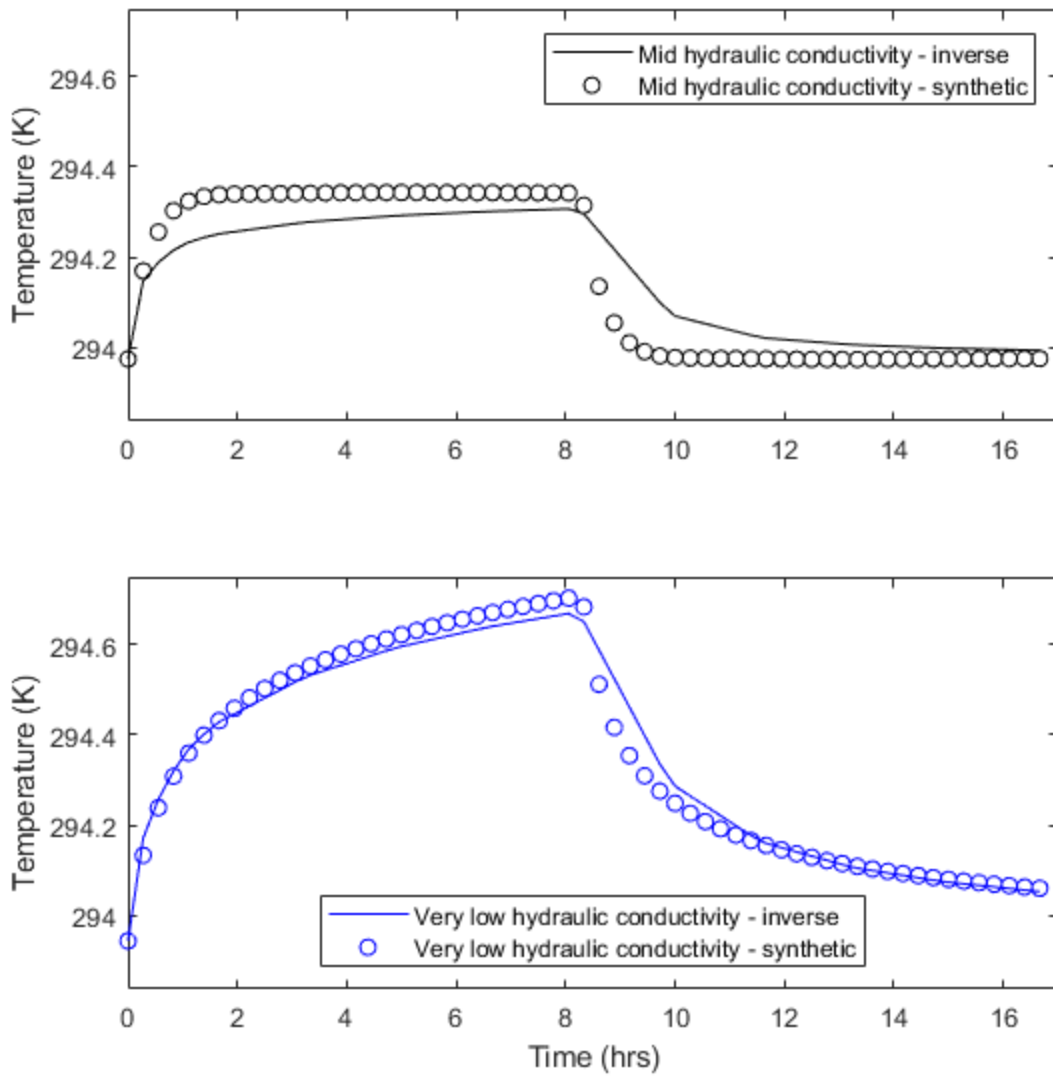


Figure 15: Temperature time series of model calculated heat transfer in model scenario v6. Shown at representative elevations of the simulated hydrostratigraphic units. The mean *RMSE* for the very low and mid hydraulic conductivity units is $2.69e-4$ and $2.11e-4$ K, respectively.

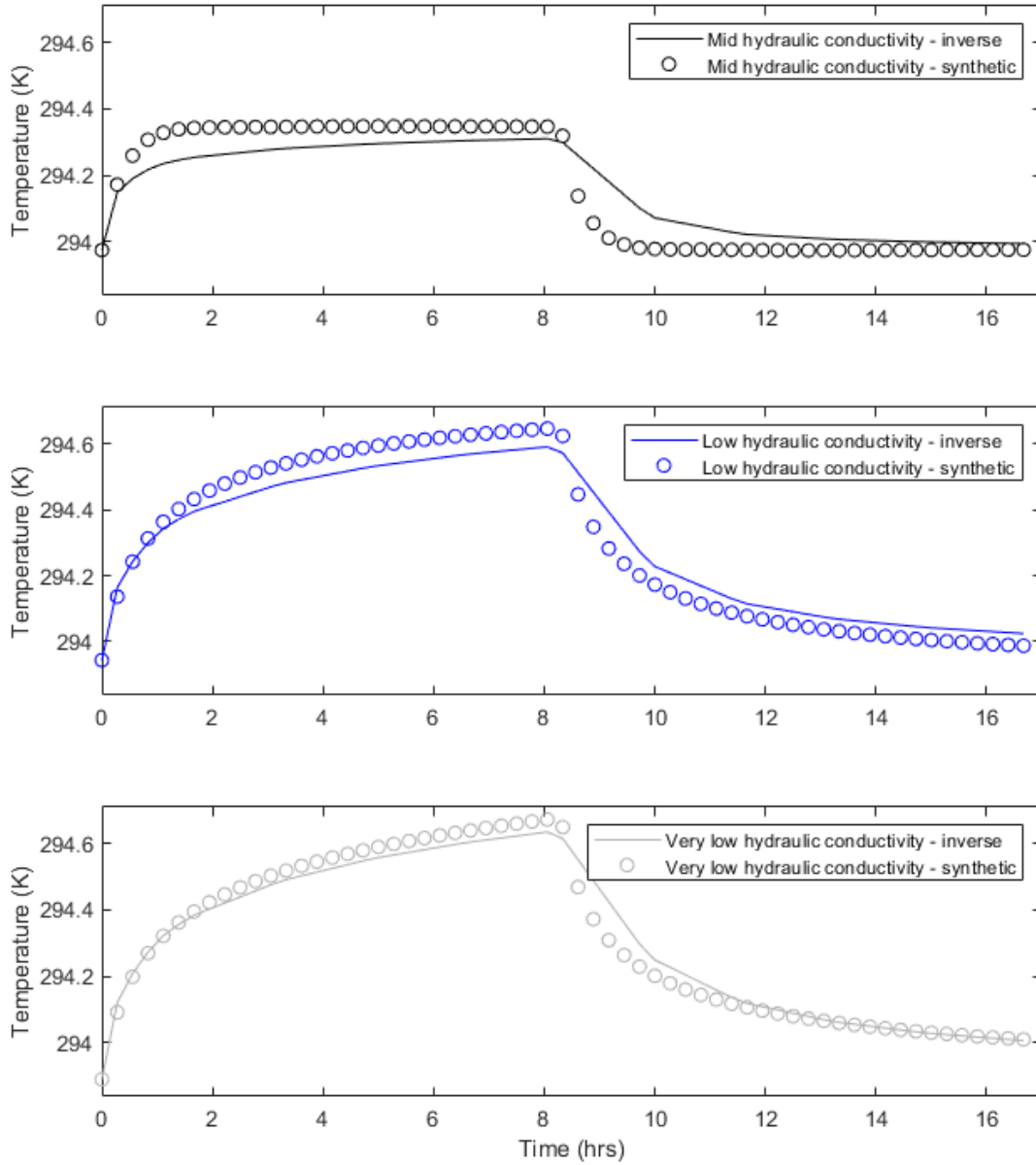


Figure 16: Temperature time series of model calculated heat transfer in model scenario v7. Shown at representative elevations of the simulated hydrostratigraphic units. The mean *RMSE* for the very low, low, and mid hydraulic conductivity units is $4.54e-4$, $2.92e-4$, and $2.80e-4$ K, respectively.

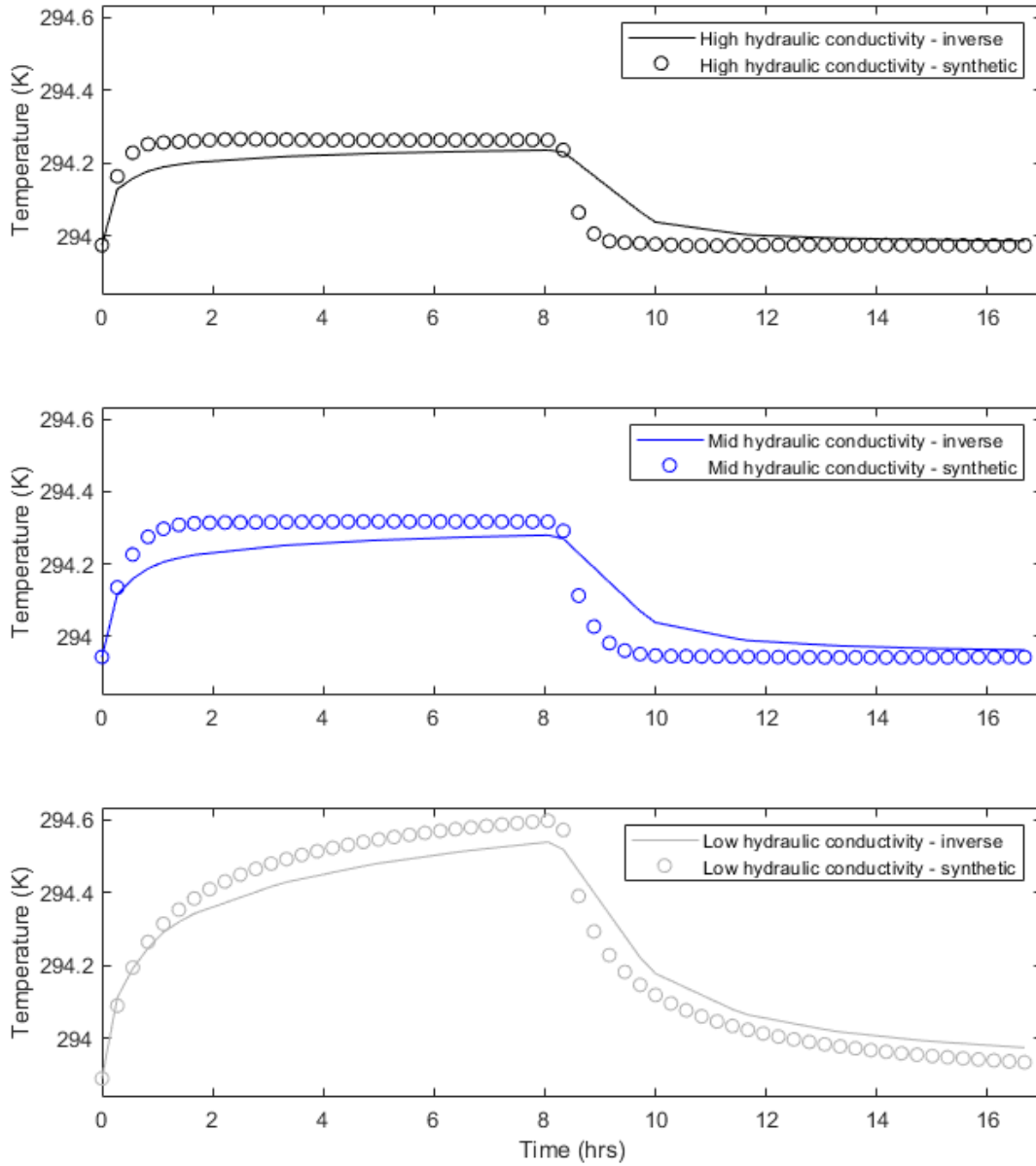


Figure 17: Temperature time series of model calculated heat transfer in model scenario v8. Shown at representative elevations of the simulated hydrostratigraphic units. The mean *RMSE* for the low, mid, and high hydraulic conductivity units is $3.26e-4$, $5.20e-4$, and $1.91e-4$ K, respectively.

REFERENCES CITED

- Anderson, M.P., 2005, Heat as a ground water tracer: *Ground Water*, v. 43(6), p. 951–968, <https://doi.org/10.1111/j.1745-6584.2005.00052.x>.
- Banks, E.W., Shanafield, M.A., and Cook, P.G., 2014, Induced Temperature Gradients to Examine Groundwater Flowpaths in Open Boreholes: *Groundwater*, v. 52, p. 943–951, <https://doi:10.1111/gwat.12157>.
- Belcher, W.R., and Sweetkind, D.S., 2010, Death Valley regional groundwater flow system, Nevada and California—Hydrogeologic framework and transient groundwater flow model: U.S. Geological Survey Professional Paper 1711, 398 p.
- Briggs, M. A., Lautz, L. K., Buckley, S. F., and Lane, J. W., 2014, Practical limitations on the use of diurnal temperature signals to quantify groundwater upwelling: *Journal of Hydrology*, v. 519, p. 1739–1751, <https://doi.org/10.1016/j.jhydrol.2014.09.030>.
- Briggs, M. A., Lautz, L. K., McKenzie, J. M., Gordon, R. P., and Hare, D. K., 2012, Using high-resolution distributed temperature sensing to quantify spatial and temporal variability in vertical hyporheic flux: *Water Resources Research*, v. 48, W02527. <https://doi.org/10.1029/2011WR011227>.
- Bredehoeft, J.D., and Papadopoulos, I.S., 1965, Rates of vertical ground-water movement estimated from the Earth's thermal profile: *Water Resources Research*, v. 2, p. 325–328.
- Cartwright, K., 1970, Groundwater discharge in the Illinois basin as suggested by temperature anomalies: *Water Resources Research*, v. 6 (3), p. 912–918.
- Darcy, H.P.G., 1856, *Les fontaines publiques de la Ville de Dijon*: Paris, France: Victon Dalmont.
- Domenico, P.A., and Schwartz, F.W., 1997, *Physical and Chemical Hydrogeology* (second edition): New York, John Wiley & Sons, Inc., 528 p.
- Fetter, C.W., 2001, *Applied Hydrogeology* (fourth edition): Upper Saddle River, New Jersey, Prentice-Hall, Inc., 598 p.
- Fischer, J.M., 1992, *Sediment Properties and Water Movement Through Shallow Unsaturated Alluvium at an Arid Site for Disposal of Low-Level Radioactive Waste Near Beatty, Nye County, Nevada*: U.S. Geological Survey Water-Resources Investigations Report 92-4032, 48 p.
- Fowler, C.M.R., 1990, *The Solid Earth: An Introduction to Global Geophysics* (first edition): New York, Cambridge University Press, 472 p.
- Fox, R.W., McDonald, A.T., and Pritchard, P.J., 2004, *Introduction to Fluid Mechanics* (sixth edition): New York, John Wiley & Sons, Inc., 800 p.

- Freifeld, B.M., Finsterle, S., Onstott, T.C., Toole, P., and Pratt, L.M., 2008, Ground surface temperature reconstructions: Using in situ estimates for thermal conductivity acquired with a fiber-optic distributed thermal perturbation sensor: *Geophysical Research Letters*, v. 35, p. 3–7, <https://doi.org/10.1029/2008GL034762>.
- Gillespie, D., 2005, Temperature Profiles and Hydrologic Implications from the Nevada Test Site Area: Prepared for Department of Energy National Nuclear Security Administration, DOE/NV/13609-40, 88 p.
- Glose, T.J., Lowry, C.S., and Hausner, M.B., 2019, Limits on groundwater-surface water fluxes derived from temperature time series: Defining resolution-based thresholds: *Water Resources Research*, v. 55, p. 10,678–10,689, <https://doi.org/10.1029/2019WR025643>.
- Goto, S., Yamano, M., and Kinoshita, M., 2005, Thermal response of sediment with vertical fluid flow to periodic temperature variation at the surface: *Journal of Geophysical Research*, v. 110, B01106, <https://doi.org/10.1029/2004JB003419>.
- Hatch, C.E., Fisher, A.T., Revenaugh, J.S., Constantz, J. and Ruehl, C., 2006, Quantifying surface water–groundwater interactions using time series analysis of streambed thermal records: Method development: *Water Resources Research*, v. 42, W10410, [doi:10.1029/2005WR004787](https://doi.org/10.1029/2005WR004787).
- Hausner, M.B., Kryder, L., Klenke, J., Reinke, R., and Tyler, S.W., 2016, Interpreting Variations in Groundwater Flows from Repeated Distributed Thermal Perturbation Tests: *Groundwater*, v. 54, p. 559–568, <https://doi.org/10.1111/gwat.12393>.
- Hoffmann, J.P., Blasch, K.W., and Ferre, T.P., 2003, Combined use of heat and soil-water content to determine stream/ground-water exchanges, Rillito Creek, Tucson, Arizona in Stonestrom and Constantz, ed., *Heat as a tool for studying the movement of ground water near streams*: U.S. Geological Survey Circular 1260, p. 47-55.
- Irvine, D.J., Lautz, L.K., Briggs, M.A., Gordon, R.P., and McKenzie, J.M., 2015, Experimental evaluation of the applicability of phase, amplitude, and combined methods to determine water flux and thermal diffusivity from temperature time series using VFLUX 2: *Journal of Hydrology*, v. 531, p. 728–737, <https://doi.org/10.1016/j.jhydrol.2015.10.054>.
- Jury, W., and Horton, R., 2004, Soil thermal regime, *in* Jury, W., and Horton, R., ed., *Soil Physics* (sixth edition): New York, John Wiley & Sons, Inc., 370 p.
- Leaf, A.T., Hart, D.J., and Bahr, J.M., 2012, Active Thermal Tracer Tests for Improved Hydrostratigraphic Characterization: *Ground Water*, v. 50, p. 726–735, <https://doi.org/10.1111/j.1745-6584.2012.00913.x>.
- Lu, N., and Ge, S., 1996, Effect of horizontal heat and fluid flow on the vertical temperature distribution in a semiconfining layer: *Water Resources Research*, v. 32 (5), p. 1449-1453.
- MATLAB, 2019, MATLAB vR2019a: Natick, Massachusetts, The MathWorks Inc.

- Precise Simulation Ltd., 2020, FEATool User's Guide v1.13: <https://www.featool.com/doc> (accessed April 29, 2020).
- Read, T., Bour, O., Bense, V., Le Borgne, T., Goderniaux, P., Klepikova, M.V., Hochreutener, R., Lavenant, N., and Boschero, V., 2013, Characterizing groundwater flow and heat transport in fractured rock using fiber-optic distributed temperature sensing: *Geophysical Research Letters*, v. 40, p. 2055–2059, <https://doi.org/10.1002/grl.50397>.
- Read, T., Bour, O., Selker, J.S., Bense, V.F., Borgne, T., Hochreutener, R., and Lavenant N., 2014, Active-Distributed Temperature Sensing to continuously quantify vertical flow in boreholes, *Water Resources Research*, v. 50, p. 3706–3713, <https://doi.org/10.1002/2014WR015273>.
- Robertson, E.C., 1998, *Thermal Properties of Rocks*: U.S. Geological Survey Open-File Report 88-441, 106 p.
- Schwartz, F.W., and Zhang, H., 2003, *Fundamentals of Ground Water*: New York, John Wiley & Sons, Inc., 583 p.
- Selker, J.S., Thevenaz, L., Huwald, H., Mallet, A., Luxemburg, W., van de Giesen, N., Stejskal, M., Zeman, J., Westhoff, M., and Parlange, M.B., 2006, Distributed fiber-optic temperature sensing for hydrologic systems: *Water Resources Research*, v. 42 (12), W12202, <https://doi.org/10.1029/2006WR005326>.
- Sellwood, S., Hart, D., Bahr, J.M., 2015, Evaluating the Use of In-Well Heat Tracer Tests to Measure Borehole Flow Rates: *Groundwater Monitoring and Remediation*, v. 35 (4), <https://doi.org/10.1111/gwmmr.12134>.
- Stallman, R.W., 1963, Computation of ground-water velocity from temperature data, in Bentall, R., ed., *Methods of Collecting and Interpreting Ground-Water Data*: U.S. Geological Survey Water Supply Paper 1544-H, p. 36-46.
- Stallman, R.W., 1965, Steady one-dimensional fluid flow in a semi-infinite porous medium with sinusoidal surface temperature: *Journal of Geophysical Research* v. 70 (12), p. 2821-2827.
- Stonestrom, D.A., and Blasch, K.W., 2003, Appendix A Determining temperature and thermal properties for heat-based studies of surface-water groundwater interactions in Stonestrom and Constantz, ed., *Heat as a tool for studying the movement of ground water near streams*: U.S. Geological Survey Circular 1260, p. 73-80.
- Suzuki, S., 1960, Percolation measurements based on heat flow through soil with special reference to paddy fields: *Journal of Geophysical Research* v. 65 (9), p. 2883–2885.
- Taniguchi, M., Turner, J.V. and Smith, A.J., 2003, Evaluations of groundwater discharge rates from subsurface temperature in Cockburn Sound, Western Australia: *Biogeochemistry* v. 66, p. 111–124.

Tyler, S.W., Selker, J.S., Hausner, M.B., Hatch, C.E., Torgersen, T., Thodal, C.E., and Schladow, S.G., 2009, Environmental temperature sensing using Raman spectra DTS fiber-optic methods: *Water Resources Research*, v. 45, p. W00D23, <https://doi.org/10.1029/2008WR007052>.

CURRICULUM VITAE

Kevin Heintz, M.S.

Email: kheintz3@gmail.com

Education:

University of Nevada, Las Vegas
M.S., Geoscience, 2022

Northern Arizona University
B.S., Geology, 2015